

MALAYSIAN

Journal of Catalysis

Vol. 8, No. 1, 2024

eISSN 0128-2581

Topics of journal (but are not limited to):

1. Catalytic Mechanisms

- 1-1. Spectroscopic and Visualizing Characterizations
- 1-2. Surface Chemistry, Reaction Kinetics and Mechanisms
- 1-3. Molecular Simulation and Theoretical Modeling
- 1-4. New Concepts for Catalysis

2. Catalytic Materials

- 2-1. Nanostructured Catalytic Materials
- 2-2. Micro- and Meso-Porous Catalytic Materials
- 2-3. Hybrid materials for catalysis

- 2-4. Novel Design and Synthetic Approaches

3. Catalysis for Energy

- 3-1. Efficient Utilization of Fossil Sources
- 3-2. Clean Energy Conversion: Electrocatalysis
- 3-3. Biomass Conversion
- 3-4. Photocatalysis for Hydrogen Production

4. Environmental Catalysis

- 4-1. Automotive Exhaust Cleanup
- 4-2. Water Pollution Control
- 4-3. Air Pollution Control
- 4-4. Updating and Utilization of Wastes

5. Catalysis for Chemical Synthesis

- 5-1. Green Synthesis
- 5-2. Petrochemicals
- 5-3. Fine Chemicals and Pharmaceuticals
- 5-4. Selective Oxidation & Hydrogenation

6. Cross-Disciplinary

- 6-1. Integration of Heterogeneous and Homogeneous
- 6-2. Organic and Biomimetic Catalysis
- 6-3. Industrial Catalysis
- 6-4. Other Surface Active Site Phenomena
- 6-5. Adsorption-Desorption Phenomena
- 6-6. Active sites Studies
- 6-7. Others

Editor-in-Chief

Prof. Dr. Aishah Abdul Jalil

Editor

- Prof. Dr. YH Taufiq Yap
- Prof. Dr. A. Zuhairi Abdullah
- Prof. Dr. Madzlan Aziz
- Assoc. Prof. Dr. Rafiziana Md Kasmani
- Asspc. Prof. Dr. Herma Dina Setiabudi
- Assoc. Prof. Dr. Wan Nor Roslam Wan Ishak
- Dr. Tuan Amran Tuan Abdullah
- Dr. Muhammad Arif Abd Aziz

Associate Editor

- Prof. Dr. Dinko Pradyoko
- Assoc. Prof. Dr. Juan Joon Ching
- Assoc. Prof. Dr. Oki Muraza
- Assoc. Prof. Dr. Sharif H. Zein
- Assoc. Prof. Dr. R. Saravanan
- Assoc. Prof. Dr. Bawadi Abdullah
- Dr. Dai-Viet N. Vo
- Dr. O.B. Oyedele
- Dr. Hambali Umar Hambali
- Dr. Muhammad Lutfi Firmnasyah
- Dr. Hasliza Bahruji
- Dr. Rohul Hayat Adnan
- Dr. Muhamad Yusuf Shahul Hamid
- Dr. Nurfatehah Wahyuni Che Jusoh
- Dr. Che Rozid Mamat
- Dr. Teh Lee Peng
- Dr. Nur Hazirah Rozali Annuar

Editorial Office & Manager

- Dr. Nurul Sahida Hassan
- Dr. Mahadi Bahari



Faculty of Chemical and Energy Engineering
Universiti Teknologi Malaysia
<http://mjcat.utm.my/>

Catalytic deoxygenation of *Reutealis trisperma* oil over Al-MCM-41 derived from red mud

Reva Edra Nugraha^{1*}, Afna Agata Zendasary², Suprpto Suprpto², Abdul Aziz², Holilah Holilah³, Didik Prasetyoko^{2*}

¹Department of Chemical Engineering, Faculty of Engineering, Universitas Pembangunan Nasional "Veteran" Jawa Timur, Surabaya, East Java, 60294, Indonesia

²Department of Chemistry, Faculty of Science and Data Analytics, Institut Teknologi Sepuluh Nopember, Keputih, Sukolilo, Surabaya, 60111, Indonesia

³Research Center for Biomass and Bioproducts, National Research and Innovation Agency of Indonesia (BRIN), Cibinong, 16911, Indonesia

*Corresponding Author: reva.edra.tk@upnjatim.ac.id; didikp@chem.its.ac.id

Article history:

Received 29 April 2024

Accepted 06 August 2024

ABSTRACT

The Al-MCM-41 was successfully synthesized from red mud as silica and alumina source. The synthesis process involved a two-step hydrothermal method using CTABr as the mesopore template. The XRD analysis shows an amorphous structure characteristic of Al-MCM-41 with uniform hexagonal pore structure. The resulting Al-MCM-41 had a high surface area of 461.37 m²/g with the high pore volume of 0.41 cc/g. Morphologically, the Al-MCM-41 catalyst displayed agglomerated small crystallites with particle sizes ranging from 0.6 to 1.4 μm. Elemental analysis showed the catalyst comprised Al, Si, Fe, and O elements, with percentages of 5.45%, 39.61%, 2.72%, and 49.09%, respectively. The catalyst was used in the catalytic deoxygenation of *Reutealis trisperma* oil to produce diesel-range hydrocarbon. Furthermore, GC-MS analysis of the liquid product demonstrated a selectivity of 48.5% for hydrocarbons and 28.14% of aromatic.

Keywords: red mud, Al-MCM-41, deoxygenation, hydrocarbon

© 2024 Faculty of Chemical and Engineering, UTM. All rights reserved
| eISSN 0128-2581 |

1. INTRODUCTION

The aluminum industry's development has led to several significant challenges, particularly in waste management. A notable issue is the production of red mud (RM) during the alumina production process using the Bayer method, resulting in brownish-red solid waste. Statistical data indicates that the global abundance of RM reached 4 billion tonnes in 2019, with an estimated annual increase of up to 150 million tonnes [1–4]. Red mud, which has a pH of roughly 10–13.3, has significant alkaline qualities. The accumulation of moist mud in rivers or ponds raises the pH of the water system since it is an alkaline waste. If red mud is directly released into the environment without being treated, it must be stored properly across a wide region to avoid negative effects on the soil and water [5]. Red mud accumulation's negative effects on the environment might be mitigated by using it as a source of minerals for chemical synthesis. Red mud contains several metal oxides like Al₂O₃, CaO, Fe₂O₃, SiO₂, TiO₂ etc [6,7]. Researchers have explored various applications of red mud, such as using it as a precursor in zeolite synthesis [7,8], mesoporous alumina [9], mesoporous aluminosilicate [10], concrete raw

materials [11], road materials [12] etc. In previous study, thermal and chemical treatments were performed to remove impurities from the red mud before its use in chemical synthesis. In the synthesis of ZSM-5, red mud is treated with NaOH to eliminate iron species that could compromise zeolite purity [13]. Some researchers have used calcination to transform the crystalline phase of red mud into an amorphous form [14]. Adding citric acid decreased the pH and total alkalinity of red mud by enhancing the solubility of Na, Ca, and Al [15].

The synthesis of acid catalysts like Al-MCM-41 has practical applications in catalytic deoxygenation reactions. Al-MCM-41's unique characteristics, including its mesoporous structure and high acid sites, enable it to significantly enhance hydrocarbon production from triglycerides. In the context of biofuel production, the catalytic deoxygenation reaction plays a crucial role. This reaction requires a catalyst to remove oxygen content from fatty acids while also inhibiting hydrocracking reactions, thereby ensuring the formation of hydrocarbons with appropriate chain lengths [16–18]. The utilization of a catalyst in the deoxygenation reaction is expected to increase

biofuel products within the C11-C18 range while reducing carbonyl compounds. The previous study reported that employing an acid catalyst with high Lewis acid sites can boost hydrocarbon products (C11-C18) while decreasing carbonyl compounds in vegetable oil [16]. Additionally, studies have indicated that the presence of Fe content in the catalyst can inhibit the C-C bond cracking reaction in the target hydrocarbon range (C11-C18), thereby enhancing catalytic activity and hydrocarbon selectivity [19]. Besides catalyst design, selecting the appropriate feedstock is also crucial for biofuel production. Non-edible oil is preferred as a feedstock over edible oil due to competition in the food sector. *Reutealis trisperma* is a promising non-edible biodiesel plant, known for its high seed production capacity and oil content. Additionally, it can thrive in unfavorable environmental conditions [20].

In this research, the Al-MCM-41 catalyst was synthesized using red mud as a source of alumina and silica. The catalytic activity of Al-MCM-41 is being investigated through the deoxygenation reaction of *Reutealis trisperma* oil

2. EXPERIMENTS

2.1 Materials

Red mud (bauxite waste) acquired from Bintan Island, Riau, Indonesia, Sodium Hydroxide (NaOH Merck, 99%), LUDOX Colloidal Silica (Sigma Aldrich 30% silica), Hexadecyltrimethylammonium bromide (CTAB, Sigma Aldrich 98%), Citric Acid (C₆H₈O₇ · H₂O, Merck 99%), n-hexane, distilled water and N₂ Ultra High Purity (UHP) gas.

2.2 Preparation of Red Mud

The red mud (RM) sample from the Bintan Islands was ground and sieved through a 125-mesh screen to achieve a finer grain size to increase the reactivity. The silica (SiO₂) in red mud was dissolve by mixing 100 mL (1 M) citric acid with 1 g red mud and stirred for 24 h. Subsequently, the mixture of red mud and citric acid (referred to as RCA) underwent centrifugation to separate the sediment. The resulting brown precipitate was then subjected to drying in an oven set at 80°C.

2.3 Synthesis of Al-MCM-41

The synthesis of Al-MCM-41 was conducted via the hydrothermal method, employing a molar composition of 10 Na₂O : 100 SiO₂ : 2 Al₂O₃ : 1800 H₂O. The molar ratio of SiO₂ to CTABr was 3.85. The RCA was used as silica source and alumina. Initially, 1.6603 g of NaOH dissolved in 19.4186 g of distilled water in a PP bottle and stirred for 30 minutes. Then, 0.7196 g of RCA was added as the silica and alumina source to the mixture. Subsequently, Ludox was gradually introduced along with distilled water to prevent clumping, and stirring continued for 8 h. After completion,

the gel mixture was left to age for 6 h at 70 °C. The first hydrothermal process occurred at 80 °C for 12 h following the aging process. CTABr was slowly incorporated into the mixture and stirred until it had a slurry texture. The second hydrothermal process took place in an autoclave at 150 °C for 24 h. The resulting solid was washed with distilled water until neutral (pH = 7) and then dried at 60 °C for 24 h. Subsequently, the dry powder underwent calcination in a tubular furnace at 550 °C (2 °C/minute) under a flow of N₂ gas for 1 h, followed by 6 h under airflow.

2.4 Catalyst Characterization

The wide X-ray Diffraction (XRD) characterization utilizing a PHILIPS-binary XPert with MPD diffractometer with Cu K radiation operating at 30 mA and 40 kV was used to examine the phase transformation of red mud to Al-MCM-41. The low XRD was performed with Bruker type D2 Phaser using KFL Cu 2K radiation at 10 mA and 30 kV to analyze the pore uniformity in Al-MCM-41. Shimadzu Instrument Spectrum One 8400S's Fourier Transform Infra-Red (FTIR) within range of 400-1400 cm⁻¹ measurement was used to examine the functional group of catalyst. The specific surface area was assessed using the Brunauer–Emmet–Teller (BET) method through N₂ Adsorption-Desorption analysis. This analysis was conducted at 363 K utilizing a Quantachrome Touchwin v1.11 instrument.

2.5 The Catalytic Deoxygenation

The deoxygenation process involved 10 g *Reutealis trisperma* oil (RTO) and 0.3 g of catalyst placed in a three-neck flask connected to distillation equipment and a heating mantle. The reaction proceeded at approximately 350 °C for 4 h. After completion of the reaction, the catalyst and residue were weighed and washed with n-hexane for catalyst reuse. The resulting deoxygenation product was weighed and subjected to analysis using Gas Chromatography-Mass Spectrometry (GC-MS). Subsequently, the Degree of Deoxygenation (DD) (Eq. 1), conversion (Eq. 2), selectivity (Eq. 3) and yield (Eq. 4) of the deoxygenation product were calculated.

Degree of deoxygenation (DD) =

$$\left[1 - \left(\frac{\%FA \text{ in liquid product}}{\%FA \text{ in reactant}} \right) \right] \times 100\% \quad \text{Eq. 1}$$

Conversion (%) =

$$\left(\frac{\text{weight of initial reactant} - \text{weight of final reactant}}{\text{weight of initial reactant}} \right) \times 100\% \quad \text{Eq. 2}$$

Selectivity =

$$\frac{(\text{peak area of desired product})}{(\text{peak area of total product})} \times 100\% \quad \text{Eq. 3}$$

Liquid yield (%) =

$$\left(\frac{\text{weight of liquid product}}{\text{weight of initial reactant}} \right) \times 100\% \quad \text{Eq. 4}$$

3. RESULTS AND DISCUSSION

3.1 Red Mud Pre-Treatment

This citric acid treatment serves to dissolve the mineral content present in red mud. According to research conducted by Kalsen et al. (2019), it demonstrates that the reduction in silica (Si) content achieved through citric acid has shown an increase compared to HCl [21]. XRD analysis was conducted to determine the crystalline phase of the sample. According to the XRD pattern depicted in Fig. 1, no notable difference was observed between RM and RCA. The diffractograms display peaks corresponding to Gibbsite ($\text{Al}(\text{OH})_3$) at $2\theta = 18.05^\circ$ and 18.10° , hematite (Fe_2O_3) at $2\theta = 24.62^\circ$, 35.75° , and 45.33° , and quartz (SiO_2) at $2\theta = 26.39^\circ$ and 26.60° [7]. A noticeable difference in peak intensity between the two diffractograms indicates crystallization within the sample. Specifically, there is a reduction in the intensity of the quartz peak in the activated red mud diffractogram, suggesting a successful separation of quartz (SiO_2) from the red mud.

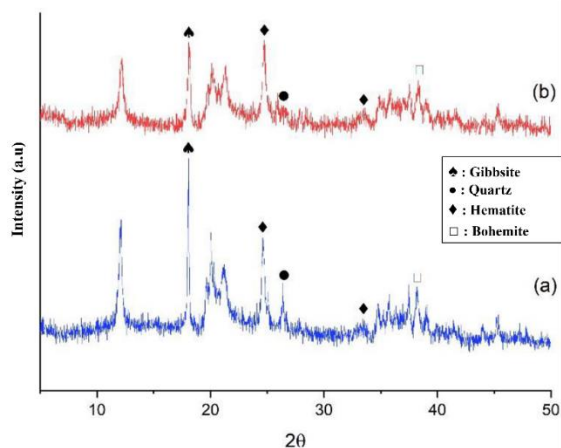


Fig. 1. Diffraction pattern of a) RM and b) RCA

The findings from the XRD analysis are further supported by the FTIR characterization of RM and RCA. In Fig. 2, the RM and RCA shows similar absorption band of Si-O, Al-O and Fe-O. The peaks are observed at wave

numbers $462 - 468 \text{ cm}^{-1}$ and $549 - 540 \text{ cm}^{-1}$, indicating bonds related to $(\text{Fe}^{3+} - \text{O}^{2-})$ which correspond to the presence of hematite (Fe_2O_3). Additionally, peaks at wave numbers $999 - 1000 \text{ cm}^{-1}$ suggest the presence of Si-O bonds from quartz, while peaks at 874 cm^{-1} , 712 cm^{-1} , and 628 cm^{-1} indicate the bond $(\text{Al}^{3+} - \text{O}^{2-})$ from Gibbsite ($\text{Al}(\text{OH})_3$) [22,23].

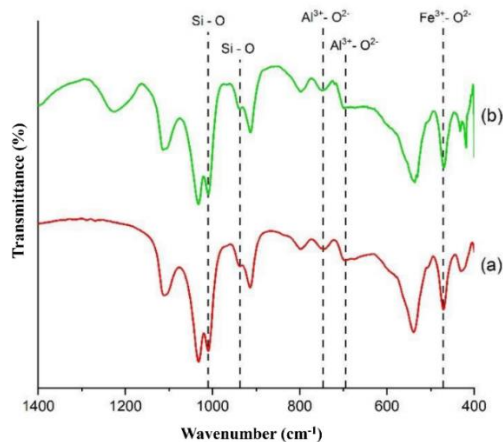


Fig. 2. FTIR spectra of a) RM and b) RCA

The results from N_2 adsorption-desorption analysis confirm that red mud is a non-porous material. The isotherm graph for both RM and RCA samples, shown in Fig. 3a, exhibits a type II isotherm according to the IUPAC classification. The type II isotherm observed in both RM and RCA indicates that they are non-porous materials [24–26]. This conclusion is further supported by the absence of hysteresis, which typically signifies the presence of condensed adsorbate liquid between non-porous particles [27]. The similarity between the two isotherms without prominent differences suggests that there is no structural change between red mud (RM) and red mud activated by citric acid (RCA).

Table 1. The textural properties of RM, RCA and Al-MCM-41

Sample	Surface area(m^2/g)			Pore volume (cc/g)			d (nm)
	S_{BET}^a	S_{micro}^b	S_{meso}^b	V_{total}^d	V_{micro}^b	V_{meso}^c	
RM	61.81	34.89	26.92	0.26	0.2	0.24	42.79
RCA	66.53	34.84	31.7	0.25	0.2	0.23	11.4
Al-MCM-41	461.73	377.38	84.35	0.41	0.04	0.37	2.5

^a S_{BET} by BET method

^b S_{micro} , S_{meso} and V_{micro} by t-plot method

^c V_{meso} by BJH desorption

^d $V_{\text{total}} = V_{\text{micro}} + V_{\text{meso}}$

The pore distribution of RM and RCA were shown in Fig. 3b. RM shows the higher pore diameter of 42.79 nm, meanwhile the RCA shows the lower pore diameter of 11.4 nm. As shown in Table 1, the RM sample has a total surface

area of 61.81 m²/g and a total pore volume of 0.26 cc/g, while the RCA sample exhibits an increased total surface area of 66.53 m²/g and a total pore volume of 0.25 cc/g.

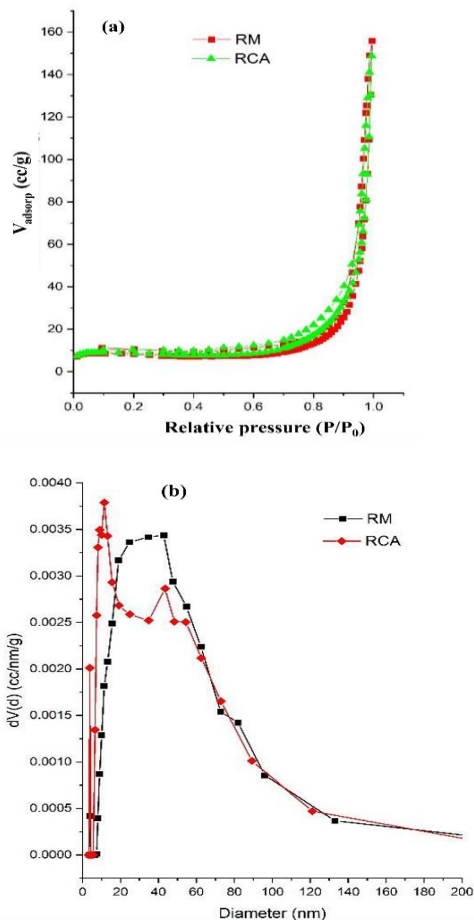


Fig. 3. The N₂ adsorption-desorption of isotherm and pore size distribution of RM and RCA

3.2 FTIR

The wide-angle XRD analysis results, as depicted in Fig. 4a reveal a broad peak at around $2\theta = 23^\circ$, indicating the formation of an amorphous structure from silica [28]. Fig. 4b, displaying the low-angle XRD pattern of the Al-MCM-41 catalyst, shows a strong peak at $2\theta = 2.2^\circ$ corresponding to the (100) plane, along with two weaker peaks at $2\theta = 3.5^\circ - 4.2^\circ$ related to the (110) and (200) plane reflections [29,30]. These peaks collectively suggest the formation of a well-structured mesoporous material consistent with the hexagonal structure of MCM-41[31]. The strong and sharp peak of the (100) plane further indicates good crystallization of the mesoporous structure [32].

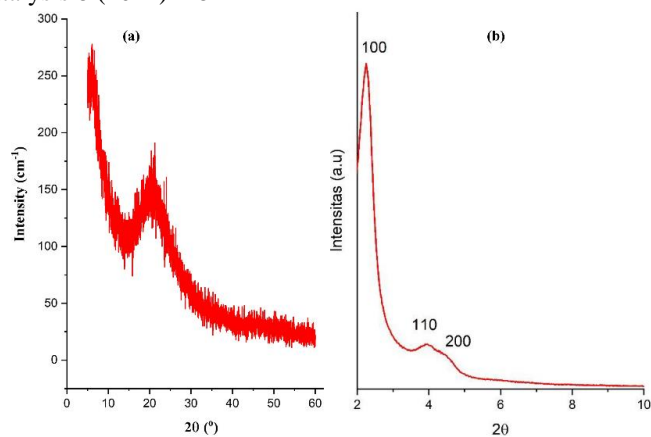


Fig. 4. The wide a) and low angle b) XRD analysis of Al-MCM-41

The FTIR spectra of Al-MCM-41 was depicted in Fig. 5 reveal a peak at a wavenumber of 457 cm⁻¹ corresponding to the Si-O vibration of TO₄ [33]. Additionally, the peak at 798 cm⁻¹ signifies the bending vibration of the Si-O-Si group [34]. The peak observed at the wavenumber of 1100 cm⁻¹ corresponds to the internal asymmetric stretching vibration of the T-O-T bond, where T can be Si or Al [35]. The peak in the range of 950-970 cm⁻¹ is typically associated with Si-OH or Si-OM⁺ vibrations [33]. Additionally, the wavenumber 1220 cm⁻¹ represents the external asymmetric stretching vibration of Si-O [36].

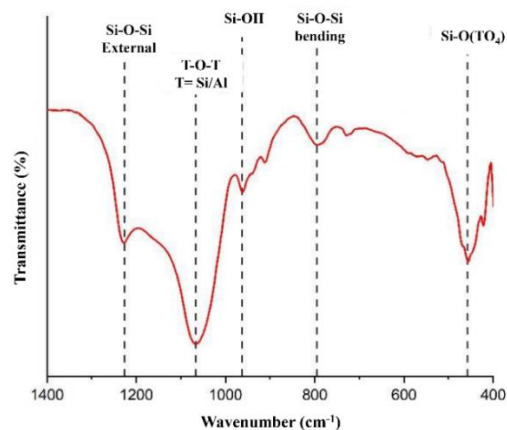


Fig. 5. FTIR spectra of Al-MCM-41

According to IUPAC, the Al-MCM-41 isotherm depicted in Fig. 6a is classified to type IV isotherm with type H1 hysteresis [37,38]. The Al-MCM-41 catalyst's isotherm shows a typical mesoporous material with hysteresis at $P/P_0 = 0.4 - 1$ [39]. The hysteresis curve is associated with the secondary capillary condensation process, which fills the pores at $P/P_0 < 1$ in mesoporous materials [40,41]. The Al-MCM-41 catalyst exhibits an H1 hysteresis type, indicating that the sample comprises plate-like particles and pores resembling gaps. This type of hysteresis is often observed in catalyst samples synthesized from clay, where the pores

resemble gaps [42]. The analysis of pore distribution in Al-MCM-41 using the BJH method (Fig. 6b) indicates that the catalyst's pore diameter ranges from 1.8 to 5.5 nm. According to Table 1, the Al-MCM-41 catalyst has a total surface area of 461.73 m²/g and a total pore volume of 0.41 cc/g. This signifies an increase in the surface area of RM and RCA on Al-MCM-41, suggesting improved catalytic activity in deoxygenation reactions.

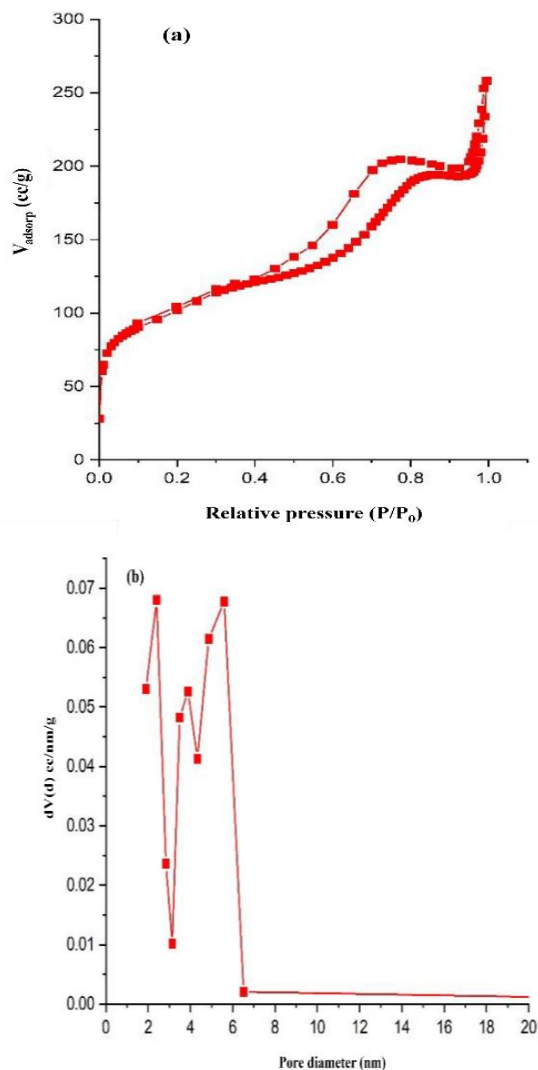


Fig. 6. a) The N₂ adsorption-desorption of isotherm and b) pore size distribution of Al-MCM-41

The SEM-EDX analysis revealed the morphology and elemental composition of the samples. The SEM profile depicted in Fig. 7 indicates that red mud has a particle size ranging from 0.4 to 1.3 μm, with irregular particle shapes. Some particles appear spherical and agglomerated [43]. On the other hand, the morphology of Al-MCM-41 shows small crystals agglomerating into larger aggregates [17]. The particle size of Al-MCM-41 ranges from 0.6 to 1.4 μm. The EDX analysis results indicate the presence of Al, Si, Fe, and O elements in both red mud and the Al-MCM-41 catalyst, as

shown in Table 2. From the table, it is evident that there was a decrease in Al content and an increase in Si content from red mud to Al-MCM-41. This change is attributed to the lower molar ratio of Al compared to Si during the synthesis of Al-MCM-41, resulting in a higher Si content in the catalyst. Similarly, there was a decrease in Fe content in Al-MCM-41 compared to red mud. This reduction in Fe content is due to the pre-treatment of the red mud material before its use in catalyst synthesis [9].

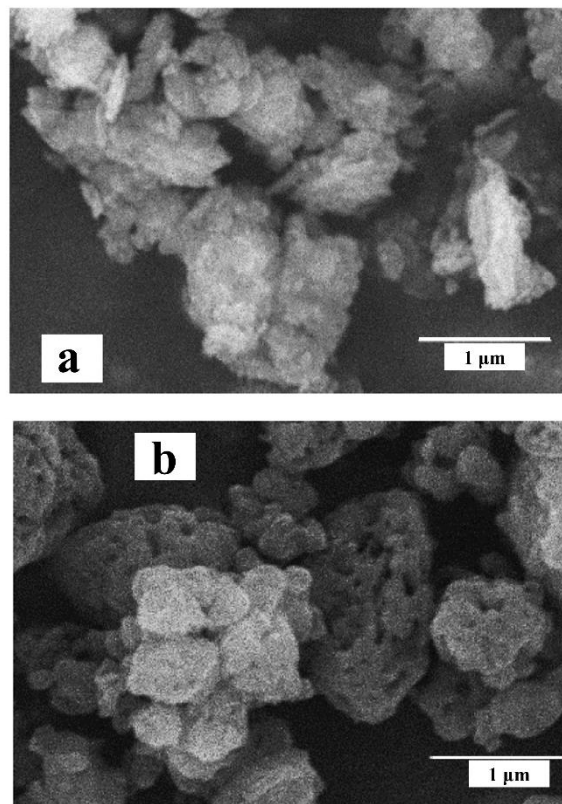


Fig. 7. The SEM images of a) RM and b) Al-MCM-41

Table 2. The EDX analysis of RM and Al-MCM-41

Element	% weight		% atom	
	RM	Al-MCM-41	RM	Al-MCM-41
Al	22.90	5.45	17.31	4.16
Si	12.95	39.61	9.40	28.99
Fe	8.01	2.72	2.93	1.00
O	54.22	49.09	69.10	63.06

3.3 Catalytic Activity

The catalytic activity was tested in the deoxygenation reaction of *Reutealis trisperma* oil. The deoxygenation reaction was carried out for 4 h at 350°C with a N₂ gas flow. In this catalytic activity test, the GC-MS instrument was utilized to perform qualitative and quantitative analysis on the deoxygenation process product. The conversion, yield and degree of deoxygenation of liquid product obtained from

different catalysts was shown in Table 3. The deoxygenation reaction of *Reutealis trisperma* oil resulted in the conversion of reactants into liquid (bio-oil), gas (CO and CO₂) and coke. According to Table 3, using RCA as a catalyst yielded the highest conversion rate at 64.45%, with a liquid yield of 33.44%. On the other hand, the Al-MCM-41 catalyst achieved a conversion rate of 45.4% with a liquid yield of 17.99%. The highest hydrocarbon selectivity was observed when using the Al-MCM-41 catalyst at 48.50%. Interestingly, even without a catalyst, the reaction showed good selectivity at 45.78%. However, the use of a catalyst notably increased the amount of oil converted and provided a higher liquid yield. This underscores the influence of acid sites and mesoporosity on the catalyst in promoting the conversion of *Reutealis trisperma* oil into hydrocarbons [44].

Table 3. Conversion, yield and degree of deoxygenation of liquid product

Catalysts	Conversion (%)	Yield (%)	Degree of Deoxygenation
Blank	41.8	9.24	45.78
RM	45.1	11.7	34.00
RCA	64.45	33.44	14.89
Al-MCM-41	45.5	17.99	48.50

The GC-MS analysis of deoxygenation liquid products reveals several data points, including the distribution of compounds from oil and the distribution of carbon chains. Figure 8, illustrates the composition of the liquid deoxygenation product, which includes hydrocarbons, cyclic compounds, aromatics, carboxylic acids, and ketones. The catalytic activity of the sample is reflected in the selectivity of hydrocarbons and compounds containing oxygen. Specifically, the Al-MCM-41 catalyst demonstrates good hydrocarbon selectivity at 48.50%, with a carboxylic acid selectivity that is 12.74% lower compared to other reactions. This lower selectivity for carboxylic acids suggests a reduction in the oxygen content of the deoxygenation product, indicating the effective conversion of oxygen-containing compounds into hydrocarbons. The activity test for the Al-MCM-41 catalyst also revealed an aromatic compound selectivity of 28.14%, which is attributed to the Brønsted acid site. In biofuel production via deoxygenation reaction, the goal is to reduce the oxygen component. Aromatic compounds can lower the freezing point, reduce the energy released during combustion, and decrease oil viscosity [45]. Therefore, achieving good hydrocarbon and aromatic selectivity is a desirable outcome in this research. The selectivity observed corresponds to the degree of deoxygenation achieved by RCA, which is 83.94% compared to the blank reaction (91.71%), RM (93.15%), and the highest with Al-MCM-41 (93.17%). The degree of deoxygenation is directly related to the reduction in the concentration of fatty acids in the liquid deoxygenation product, thereby impacting its composition [46].

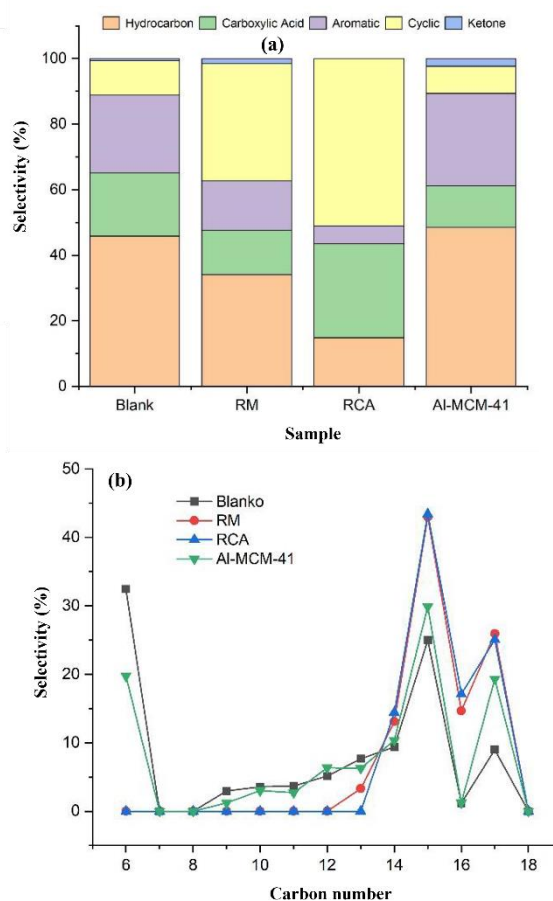


Fig. 8. Hydrocarbon distribution from catalytic deoxygenation reaction of *Reutealis trisperma* oil

The deoxygenation process results in oxygen-free hydrocarbons with one fewer carbon atom than the original fatty acid (C₁₆₋₁₈). These hydrocarbons are categorized into short carbon chains (C₆₋₁₀) and long carbon chains (C₁₁₋₁₇). Fig. 8b illustrates the carbon chain distribution, showing that when using Al-MCM-41 as the catalyst, the deoxygenation product comprises 24% short carbon chains (C₆₋₁₀) and 76% long carbon chains (C₁₁₋₁₇), with the primary product being (C₁₅+C₁₇) at 49.2%. This indicates successful deoxygenation of RTO with this catalyst. In the deoxygenation of *Reutealis trisperma* oil using the Al-MCM-41 catalyst, there is a significant formation of short-chain hydrocarbons (C₆₋₁₀). This formation of short-chain hydrocarbon products is believed to result from a secondary hydrocracking reaction. The catalyst's characteristics, especially a higher concentration of Brønsted acid compared to Lewis acid, can indeed trigger hydrocracking reactions, resulting in a higher yield of short-chain hydrocarbons (C₈₋₁₀) [47,48]. The catalyst's characteristics, especially a higher concentration of Brønsted acid compared to Lewis acid, can indeed trigger hydrocracking reactions, resulting in a higher yield of short-chain hydrocarbons (C₈₋₁₀). This is because Brønsted acid sites are known to promote hydrocracking reactions, which break down larger hydrocarbons into smaller ones, thus favoring the production of shorter carbon chain compounds

[16]. This is because Brønsted acid sites are known to promote hydrocracking reactions, which break down larger hydrocarbons into smaller ones, thus favoring the production of shorter carbon chain compounds.

4. CONCLUSION

The Al-MCM-41 catalyst derived from red mud has been successfully synthesized. This catalyst boasts a substantial total surface area of 461.73 m²/g, with a mesopore surface area measuring 84.35 m²/g and a mesopore volume of 0.37 cc/g. Featuring a pore diameter of 2.5 nm, the morphology of Al-MCM-41 reveals the agglomeration of small crystals into larger aggregates, presenting a particle size range of 0.6 – 1.4 μm. The elemental composition showcases the presence of Al (5.45%), Si (39.61%), Fe (2.72%), and O (49.09%). In catalytic tests involving the deoxygenation reaction of *Reutealis trisperma* oil, the Al-MCM-41 catalyst demonstrated a remarkable hydrocarbon selectivity of 48.5%, alongside a notably low carboxylic acid selectivity of 12.74% compared to alternative catalysts utilized in similar reactions.

ACKNOWLEDGEMENTS

The authors acknowledge the Ministry of Education, Culture, Research, and Technology of Republic Indonesia under PDUPT research grant with contract number 1209/PKS/ITS/2023 for funding the research and Universitas Pembangunan Nasional “Veteran” Jawa Timur under Penelitian Dasar Lanjutan scheme with contract number of SPP/130/UN.63.8/LT/V/2024 for funding the research.

REFERENCES

- [1] P.B. Cusack, M.G. Healy, P.C. Ryan, I.T. Burke, L.M.T. O’ Donoghue, É. Ujaczki, R. Courtney, 179 (2018) 217–224. <https://doi.org/10.1016/j.jclepro.2018.01.092>.
- [2] K. Evans, (2016) 316–331. <https://doi.org/10.1007/s40831-016-0060-x>.
- [3] P.S. Reddy, N.G. Reddy, V.Z. Serjun, B. Mohanty, S.K. Das, K.R. Reddy, B.H. Rao, , Springer Netherlands, 2021. <https://doi.org/10.1007/s12649-020-01089-z>.
- [4] L. Wang, G. Hu, F. Lyu, T. Yue, H. Tang, H. Han, Y. Yang, R. Liu, W. Sun, (2019). <https://doi.org/10.3390/min9050281>.
- [5] E.P. Ramdhani, E. Santoso, H. Holilah, R.E. Nugraha, H. Bahruji, S. Suprpto, A.A. Jalil, N. Asikin-Mijan, S. Akhlus, D. Prasetyoko, (2023) 31989–31999. <https://doi.org/10.1039/d3ra05910c>.
- [6] H. Jahromi, F.A. Agblevor, (2018) 1–12. <https://doi.org/10.1016/j.apcatb.2018.05.008>.
- [7] H. Tehubijuluw, R. Subagyo, M.F. Yulita, R.E. Nugraha, Y. Kusumawati, H. Bahruji, A.A. Jalil, H. Hartati, D. Prasetyoko, (2021) 1–17.

- [8] C. Belviso, A. Kharchenko, E. Agostinelli, F. Cavalcante, D. Peddis, G. Varvaro, N. Yaacoub, S. Mintova, (2018) 24–29. <https://doi.org/10.1016/j.micromeso.2018.04.038>.
- [9] E.P. Ramdhani, T. Wahyuni, Y.L. Ni’mah, Suprpto, D. Prasetyoko, (2018) 337–343. <https://doi.org/10.22146/ijc.25108>.
- [10] F. Wulandari, E.P. Ramdhani, Y.L. Ni’mah, A.A. Dawam, D. Prasetyoko, (2018) 580–586. <https://doi.org/10.22146/ijc.25184>.
- [11] W.C. Tang, Z. Wang, S.W. Donne, M. Forghani, Y. Liu, (2019) 120802. <https://doi.org/10.1016/j.jhazmat.2019.120802>.
- [12] J. Zhang, Z. Yao, K. Wang, F. Wang, H. Jiang, M. Liang, J. Wei, G. Airey, (2021) 121419. <https://doi.org/10.1016/j.conbuildmat.2020.121419>.
- [13] R. Subagyo, H. Tehubijuluw, W.P. Utomo, H.D. Rizqi, Y. Kusumawati, H. Bahruji, D. Prasetyoko, (2022) 103754. <https://doi.org/10.1016/j.arabj.2022.103754>.
- [14] M. HM Ahmed, N. Batalha, Z.A. ALOthman, Y. Yamauchi, Y. Valentino Kaneti, M. Konarova, (2022) 132965. <https://doi.org/10.1016/j.cej.2021.132965>.
- [15] X. Kong, M. Li, S. Xue, W. Hartley, C. Chen, C. Wu, X. Li, Y. Li, (2017) 382–390. <https://doi.org/10.1016/j.jhazmat.2016.10.073>.
- [16] R.E. Nugraha, D. Prasetyoko, Hasliza Bahruji, Suprpto Suprpto, Nurul Asikin-Mijan, T. Prapti Oetami, A. Abdul Jalil, D.-V. N. Vo, Y. Hin Taufiq-Yap, (2021) 21885–21896. <https://doi.org/10.1039/D1RA03145G>.
- [17] R.E. Nugraha, D. Prasetyoko, N. Asikin-Mijan, H. Bahruji, S. Suprpto, Y.H. Taufiq-Yap, A.A. Jalil, (2021) 110917. <https://doi.org/10.1016/j.micromeso.2021.110917>.
- [18] K. de Sousa Castro, L. Fernando de Medeiros Costa, V.J. Fernandes, R. de Oliveira Lima, A. Mabel de Morais Araújo, M.C. Sousa de Sant’Anna, N. Albuquerque dos Santos, A.D. Gondim, (2020) 555–564. <https://doi.org/10.1039/d0ra06122k>.
- [19] J. Zhong, Q. Deng, T. Cai, X. Li, R. Gao, J. Wang, Z. Zeng, G. Dai, S. Deng, (2021) 18–21. <https://doi.org/10.1016/j.fuel.2021.120248>.
- [20] H. Hamim, M. Hilmi, D. Pranowo, D. Saprudin, L. Setyaningsih, (2017) 423–435. <https://doi.org/10.3923/pjbs.2017.423.435>.
- [21] T.S. Atalay Kalsen, H.B. Karadağ, Y.R. Eker, I. Kerti, (2019) 482–496. <https://doi.org/10.1007/s40831-019-00236-8>.
- [22] M. Mokhatr Mohamed, H. El-Faramawy, (2021) 120741. <https://doi.org/10.1016/j.fuel.2021.120741>.
- [23] S. Singh, M.U. Aswath, R. Das Biswas, R. V. Ranganath, H.K. Choudhary, R. Kumar, B. Sahoo,

- (2019) e00266. [42] O. Riski, D. Prasetyoko, D.K. Febrianti, Y.L. Nikmah, V.N. Iftitahiyah, H. Hartati, I. Qoniah, E. Santoso, (2019) 93–98. <https://doi.org/10.11113/mjfas.v15n2019.1003>.
- [24] I. V. Melnyk, V. V. Tomina, N. V. Stolyarchuk, G.A. Seisenbaeva, V.G. Kessler, (2021) 116301. <https://doi.org/10.1016/j.molliq.2021.116301>.
- [25] P. Ehiomogue, I.I. Ahuchaogu, I.E. Ahaneku, (2022) 87–96. <https://www.researchgate.net/publication/358271705>.
- [26] S.P. Rigby, 2020. <https://doi.org/10.1007/978-3-030-47418-8>.
- [27] A. Milenković, I. Smičiklas, M. Šljivić-Ivanović, N. Vukelić, (2015) 2461–2465. <https://doi.org/10.1134/S0036024415130269>.
- [28] N.T.T. Tran, Y. Uemura, S. Chowdhury, A. Ramli, (2016) 93–100. <https://doi.org/10.1016/j.apcata.2015.12.021>.
- [29] M. Hachemaoui, C.B. Molina, C. Belver, J. Bedia, A. Mokhtar, R. Hamacha, B. Boukoussa, (2021) 1–17. <https://doi.org/10.3390/catal11020219>.
- [30] H. Douba, O. Mohammedi, B. Cheknane, (2022) 569–582. <https://doi.org/10.15255/kui.2022.001>.
- [31] S. Zhao, Z. Zhang, K. Zhu, J. Chen, (2017) 388–397. <https://doi.org/10.1016/j.apsusc.2017.02.016>.
- [32] F. Mahmoudi, M.M. Amini, (2020) 101227. <https://doi.org/10.1016/j.jwpe.2020.101227>.
- [33] S.T. Pham, M.B. Nguyen, G.H. Le, T.D. Nguyen, C.D. Pham, T.S. Le, T.A. Vu, (2021). <https://doi.org/10.1016/j.chemosphere.2020.129062>.
- [34] M.S. Abdel Salam, M.A. Betiha, S.A. Shaban, A.M. Elsabagh, R.M. Abd El-Aal, F.Y. El kady, (2015) 49–57. <https://doi.org/10.1016/j.ejpe.2015.02.005>.
- [35] Y. Yue, Y. Kang, Y. Bai, L. Gu, H. Liu, J. Bao, T. Wang, P. Yuan, H. Zhu, Z. Bai, X. Bao, (2018) 177–185. <https://doi.org/10.1016/j.clay.2018.03.025>.
- [36] W.E. Rashwan, K.S. Abou-El-Sherbini, M.A. Wahba, S.A. Sayed Ahmed, P.G. Weidler, (2020) 2017–2029. <https://doi.org/10.1007/s12633-019-00262-x>.
- [37] P. López-Aranguren, S. Builes, J. Fraile, A. López-Periago, L.F. Vega, C. Domingo, (2015) 104943–104953. <https://doi.org/10.1039/c5ra20583b>.
- [38] G. Calzaferri, S.H. Gallagher, S. Lustenberger, F. Walther, D. Brühwiler, (2023) 127121. <https://doi.org/10.1016/j.matchemphys.2022.127121>.
- [39] F.C.M. Silva, M.S. Lima, C.O.C. Neto, J.L.S. Sá, L.D. Souza, (2018) 159–167. <https://doi.org/10.1007/s13399-017-0263-9>.
- [40] S. Mousa, K. Baron, R.S. Fletcher, S.P. Rigby, (2022) 130026. <https://doi.org/10.1016/j.colsurfa.2022.130026>.
- [41] M.I.H.S. N., C. Panatarani, F. Faizal, C. Mulyana, I.M. Joni, (2023) 101637.

Effect of Tea Waste Extract Volume on Synthesis of TiO₂ Nanoparticles for Photodegradation of 2,4-dichlorophenol

Nadiatul Asma Adnan¹, Nur Farhana Jaafar^{1,*}, Endang Tri Wahyuni², Auni Afifah Abdul Mutalib¹, Tasnim Aisya Mahmuelee Torlaema¹

¹ School of Chemical Sciences, Universiti Sains Malaysia, 11800 USM Penang, Malaysia

² Chemistry Department, Faculty of Mathematic and Natural Sciences, Gadjah Mada University, Sekip Utara, POB BLS 21, Yogyakarta, 55281, Indonesia

*Corresponding Author: nurfarhana@usm.my

Article history:

Received 05 August 2024

Accepted 22 September 2024

ABSTRACT

Tea is one of the most consumed drinks nowadays due to its exceptional benefits but the increase in demand of tea production has caused an impressive amount of tea waste. It has been known that plant extract containing biochemical which can be used as capping agent for synthesis of nanoparticles. In this study, the effect of volume on tea waste extract in synthesis of titanium dioxide (TiO₂) nanoparticles was investigated. 1, 3 and 5 mL of tea waste extract was selected as the extract volume which denoted as TiO₂-1, TiO₂-3 and TiO₂-5, respectively. The catalysts were characterized by XRD, FTIR, BET, UV-Vis DRS and FESEM. The results show that increasing volume of tea extract increased the band gap and crystallite size, while the surface area was decreased. The role of tea waste extract in formation of TiO₂ nanoparticles was tested to degrade 2,4-dichlorophenol (2,4-DCP) under visible light irradiation. The best photocatalytic degradation of 2,4-DCP was achieved using TiO₂-1 (85%) compared with TiO₂-3 (80%), TiO₂-5 (77%) and P25 (71%) concluded that the optimum volume of tea waste extract was 1 mL. Overall, the role of tea waste extract as capping agent in synthesis of TiO₂ nanoparticles shows that it has a good potential for replacement any organic capping agent.

Keywords: Tea waste extract; TiO₂ nanoparticles; Extract volume; Photocatalytic degradation; 2,4-dichlorophenol

© 2024 Faculty of Chemical and Engineering, UTM. All rights reserved

| eISSN 0128-2581 |

1. INTRODUCTION

Clean water is one of the crucial things in our lives, making accessibility to cleaner water a challenge as most of the water these days is heavily polluted with organic and inorganic pollutants. Few persistent organic contaminants in pharmaceuticals, pesticides, personal care products, endocrine disruptors have been found in wastewater effluents on a regular basis [1]. Chlorophenol compounds are generally used in various manufacturing industries especially for the mass production of paints, textiles, pharmaceuticals, petrochemicals and synthetic dyes [2]. Among them, 2,4-dichlorophenol (2,4-DCP) usually functioned as an intermediate for herbicides. The negative effects of phenolic chemicals on the human neurological system have been described and connected to a variety of health problems, including renal failure, liver damage, and lung damage [3]. To prevent future environmental concerns, effective treatment technologies are needed.

The photocatalysis process employing semiconductors is now thought to be advantageous in the degradation of organic pollutants because this process does

not require additional chemicals [4]. Within the last forty years, heterogeneous photocatalysis has seen numerous advances, particularly regarding energy and the environment. Titanium dioxide (TiO₂) nanoparticles have become a prospective material in photocatalytic processes due to its excellent qualities, such as its high photodegradation activity, great chemical stability, cheap and non-hazardous. Various synthetic methodologies are utilized to obtain TiO₂ nanoparticles such as physical, chemical and green synthesis method. The physical and chemical methods have a few downsides, including the need for expensive equipment, high temperatures and pressures, as well as the need for sufficient space to set up the reaction [1,4]. The use of toxic substances that are thought to be detrimental for the environment is frequently made by a chemical route synthesis and it also involves sophisticated process.

Biochemical in various plants can help in assisting the production of nanoparticles. It can be facilitated by a range of metabolites found in plant leaf extracts, which are convenient, safe to use, and easily accessible. Additionally, it is believed that extracts of plant leaf function as both

reducing and stabilizing agents to aid in the creation of nanoparticles [5]. The composition of the leaf extract affects how nanoparticles are formed. This is because different leaf extracts have variable quantities of biochemical reducing agents [6]. Additionally, some key phytochemicals implicated in the production of nanoparticles include amides, ketones, aldehydes, terpenoids and flavones [7]. The creation of nanoparticles using plant extracts is also quite novel and provides true green chemistry at a very cost-effective way [8]. To minimize the agglomeration effect and reduce the average particle size for an overall improvement in performance, TiO₂ nanoparticles can be synthesized with a variety of capping agents.

Bio-capping agents offer a one-step, cost-effective, synthesis of nanoparticles that is friendly which is sustainable and easy to scale up to industrial manufacturing. A range of synthetic processes, including eco-friendly, chemical, and physical can be used to create TiO₂ nanoparticles. Metal oxide nanoparticles' synthesis has lately switched to green biological routes that use plant-based capping agents in comparison with physical and chemical approaches which are costly and environmentally dangerous due to the use of hazardous chemicals, as well as require complex processes [9]. Previously, tea waste extracts containing phenolic and flavonoid as capping agent was used as alternative solvent for synthesis of ZnO using electrolysis method [10]. Thus, in this study the use tea wastes as plant extract in synthesis of TiO₂ nanoparticles as the alternative method which highlighted the green method. The effect of tea wastes extract volume was studied on formation of TiO₂ nanoparticles and their photoactivity was studied using 2,4-DCP under visible light irradiation.

2. MATERIAL AND METHOD

2.1 Materials

Tea wastes were obtained from cafeteria in Universiti Sains Malaysia in Penang, Malaysia. Titanium (IV) butoxide (TBOT) (97% purity), titanium P25 and 2,4-dichlorophenol (2,4-DCP) was purchased from Sigma-Aldrich (Greece). Ethanol (99.7% purity), hydrochloric acid (HCl) and sodium hydroxide (NaOH) were acquired from R&M Chemicals (Malaysia). All the materials were of an analytically pure quality and were used directly without any purification needed.

2.2 Preparation of Tea Leaves Extract

Tea waste extract was prepared using 100 g of tea leaves wastes in 200 ml of distilled water. The mixture was heated at 60°C and stirred for 10-15 minutes to ensure homogeneity. After that, the solution was left to cool before filtering the extract.

2.3 Preparation of Catalyst

The TiO₂ nanoparticles were prepared by adding 50 ml distilled water and 1 ml of tea waste extract. Then, NaOH was added dropwise into the solution until pH 12 was achieved before stirring for 30 minutes. After that, 0.3 ml of TBOT was added into solution and the mixture was left to stir at room temperature for another 3 hours follow by centrifuging the resulting suspension for 10 minutes at 3500 rpm. The precipitate was filtered and washed with distilled water repeatedly followed by ethanol. The product was dried overnight at 90°C in an oven continued by calcination at 550°C for 3 hours and the catalyst was denoted as TiO₂-1. The same procedure was repeated by changing the volume of tea waste extract to 3 and 5 ml and denoted as TiO₂-3 and TiO₂-5, respectively. In this study, commercial TiO₂ known as P25 was used as the control for synthesized catalysts.

2.3 Material Characterization

The crystalline structures of each catalyst were determined using a Bruker Advance D8 X-ray powder diffractometer (XRD) with Cu K α radiation ($\lambda = 1.5418 \text{ \AA}$). The bandgap of the catalysts was determined in the air at room temperature using a UV-Vis DRS (Perkin Elmer Lambda 900) spectrophotometer. The morphology of catalysts was observed using FEI Quanta FEG 650 Field-Emission Scanning Electron Microscope (FESEM) (Holland). Fourier transfer infrared spectroscopy (FTIR) (Perkin Elmer Spectrum 2000 FT-IR) was used to observe and identify the chemical functional groups present in the catalysts. The surface area was determined using the Brunnauer-Emmett-Teller method (BET).

2.3 Photocatalytic Degradation of 2,4-dichlorophenol

A 100 mL of 10 ppm 2,4-DCP solution was transferred into 250 mL beaker containing 0.019 g catalyst. The solution was stirred continuously in the dark for 1 hour to reach the adsorption-desorption equilibrium before being exposed under visible light irradiation for another 7 hours. The experiment was performed in a photoreactor accommodating 4 low-wattage fluorescent lamps (9 Watt, 385 nm) as the sources of the visible light irradiation. The visible lamps light source was placed 10 cm around the solution. A 3 mL of sample solution was taken within 30 minutes interval. Then, the samples were centrifuged at 9000 rpm for 15 minutes before being analyzed using UV-Vis spectrophotometer at 284 nm. Every experiment was carried out in triplicate to improve accuracy. The degradation percentage was calculated using the following equation:

Degradation efficiency (%) =

$$\frac{\text{Initial concentration} - \text{Final concentration}}{\text{Initial concentration}} \times 100\% \quad (1)$$

3. RESULTS AND DISCUSSION

Figure 1 shows the XRD patterns of P25 and TiO₂ nanoparticles synthesized using different volumes of tea waste extract. Peaks at 25.40°, 36.88°, 37.99°, 47.73°, 54.03°, 55.30°, 62.70°, 67.23°, 70.29° and 75.04° which corresponded to (101), (004), (112), (200), (105), (211), (204), (116), (220) and (215) planes, respectively were observed for all catalysts indicated the peaks of TiO₂ anatase. All catalysts showed sharp peaks indicating that there is high crystallinity in their structures. Rutile peaks can only be observed for P25 (Figure 1a) at 29.11° and 55.30° corresponding to (110) and (220) planes, respectively. All synthesized catalysts only consist of anatase phase due to the calcination temperature in this study which was 550°C. Calcination temperature played an important role in determination of the catalysts' phase. It was reported that anatase transformation to rutile phase started at 600°C [11]. Calcination not only helps to further accelerate the degree of crystallization, but it can also help to promote the order of structure in the catalysts [12].

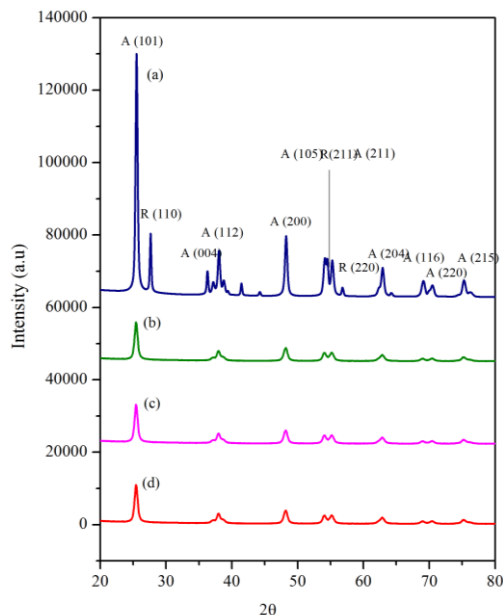


Figure 1. XRD diffractograms of (a) P25, (b) TiO₂-1, (c) TiO₂-3 and (d) TiO₂-5

Table 1. Textural analysis of the catalysts.

Catalyst	Polymorphic Phase	^a Crystallite Size (nm)	Surface area (mg ² g ⁻¹)	^b Band gap (eV)
P25	101	22.4	4.21	3.4
TiO ₂ -1	101	21.3	8.09	3.2
TiO ₂ -3	101	23.6	7.04	3.3
TiO ₂ -5	101	24.9	6.59	3.4

^aCrystallite size calculated using Debye–Scherrer equation at $2\theta = 25.4^\circ$

^bBand gap calculated using Tauc plot $eV = \frac{hc}{\lambda}$

Table 1 listed the textural properties of the catalysts. Among them, TiO₂-1 illustrated the smallest crystallite size and band gap while the highest surface area compared to others. These results due to higher volume of tea waste extract caused agglomeration which increases the particle size consequently decreasing the surface area [13].

Figure 2 shows the chemical properties of all catalysts in the range of 3500-550 cm⁻¹. Bands at 3420 cm⁻¹, 1269 cm⁻¹ and 1029 cm⁻¹ were attributed to the O-H stretching of surface-adsorbed water, hydroxyl (OH) functional groups in alcohols and phenolic compounds and C–O stretching in amino acid, respectively. The strong band at 600 cm⁻¹ and 900 cm⁻¹ showed the formation of Ti–O and Ti–O–Ti bending vibrations, respectively. The metal oxide bonds like Ti–O–Ti and Ti–O confirmed the existence of TiO₂ in the prepared TiO₂ nanoparticles [14]. The presence of the Ti–O–Ti bond is due to the strong interaction (capped) of biomolecules with TiO₂ nanoparticles which resulted in the presence of polyphenols including flavonoids, and catechins. These plant compounds were responsible in reduction process of TiO₂ nanoparticles in green synthesis [15].

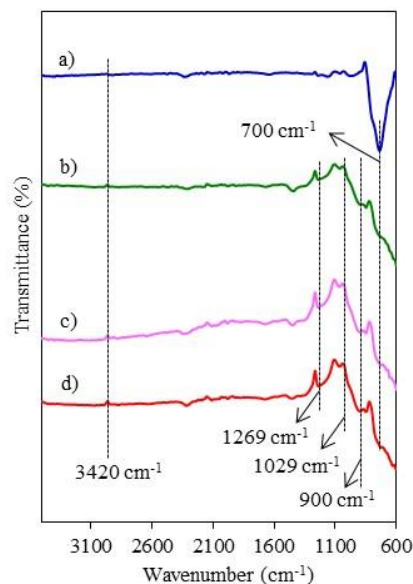


Figure 2. FTIR spectra of (a) P25, (b) TiO₂-1, (c) TiO₂-3 and (d) TiO₂-5

FESEM was used to study the surface morphology of the as shown in Figure 3. All catalysts seemed to be spherical and were non-uniform in shape and size like previous studies [16]. The FESEM images illustrated that increasing volume of tea waste extract caused the particles possibly to tend to agglomerate, and the solution started to form aggregates [17]. This agglomeration could happen because smaller particles diffuse through the solution. The diffusion that occurred added to the surface of other nuclei or nanoparticles which is regarded as growth by ripening [18]. Phytochemicals act as reducing and capping agent that helps to reduce agglomeration by controlling the morphology as well as protecting and stabilizing the catalyst. Oxygen atom

of phenolic hydroxyl group moiety bind with metal by chelating effect to form metal-phenolate hydroxyl complex [19]. Black tea's polyphenols, catechins, and caffeine are examples of water-soluble phytochemicals that are effective at reducing metal ions and forming stable, capped metallic nanoparticles [20]. From the figure, TiO₂-1 shows the smallest particle size compared to TiO₂-3 and TiO₂-5 due to less amount of OH⁻. These findings were in correlation with results in Table 1.

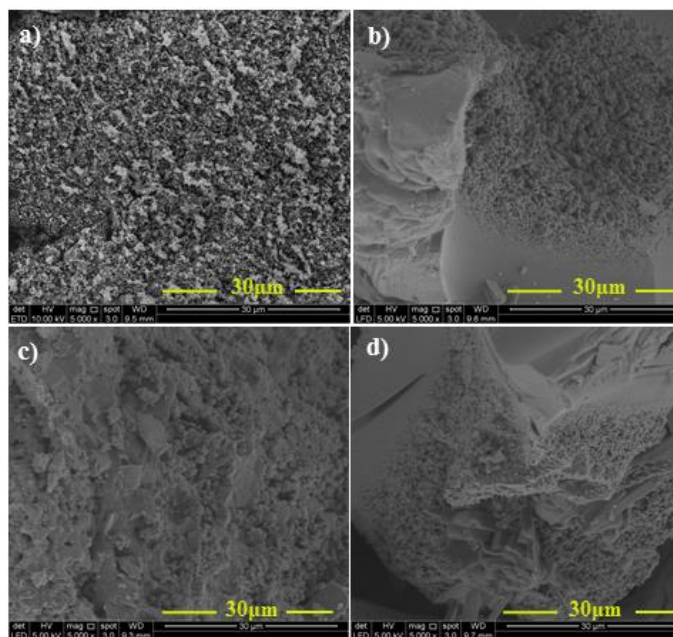


Figure 3. FESEM images of (a) P25, (b) TiO₂-1, (c) TiO₂-3 and (d) TiO₂-5.

The photocatalytic activity of the catalysts was tested using photodegradation of 2,4-DCP as shown in Figure 4. As control, photolysis was tested and the result showed that only 13% degradation of 2,4-DCP indicating the role of catalyst to this reaction. TiO₂-1 shows the highest degradation with 85% compared with TiO₂-3 (80%), TiO₂-5 (77%) and P25 (71%). The highest degradation was achieved with TiO₂ nanoparticles prepared using 1 mL tea waste extract illustrated that 1 mL is a sufficient volume for reduction and capping. In addition, adsorption study using TiO₂-1 was done for 8 hours with the absence of light resulting in only 15% degradation of 2,4-DCP indicating the importance of light source to this reaction. This result shows that variation in the biological materials is the main factor that greatly influenced the green synthesis of catalysts. The manipulation of quantity or volume of the plant extract used could alter the size and morphology of the nanostructure. Optimum quantity is needed as too low results in incomplete capping ability and too high can cause agglomeration. This statement is supported by FESEM analysis which increasing the amount of plant extract caused the nanoparticles to be agglomerated, which results in blocking of pore that lowered the surface area and limits the active sites for photodegradation. In addition, these results show that band

gap, surface area and crystallite size have synergetic effects in photoactivity of the TiO₂ nanoparticles.

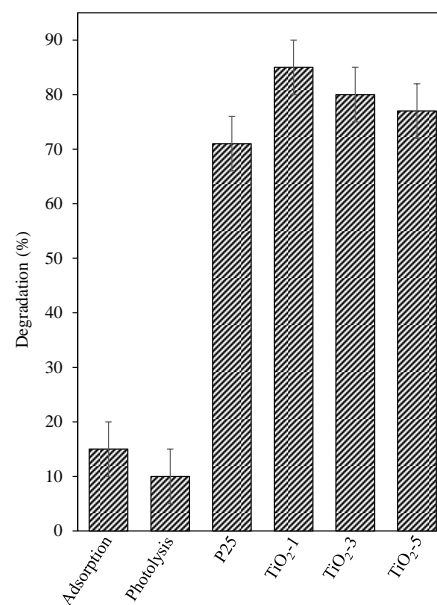


Figure 4. Adsorption and photocatalytic performances of the catalysts ($C_{2,4\text{-DCP}} = 10$ ppm, pH = 3, W = 0.019 g, t = 8 h).

4. CONCLUSION

The TiO₂ nanoparticles with different volumes of tea waste extract was successfully synthesized and used as a photocatalyst to degrade 2,4- DCP. The catalysts were characterized by XRD, FTIR, BET, UV-Vis DRS and FESEM. XRD analysis showed that all synthesized catalysts were in the anatase phase and crystallite size increased when the volume of tea waste extract increased. The bandgap energy of TiO₂ increases when tea waste volume increases from 1 mL to 5 mL. In contrast, surface area decreases with increasing volume of tea waste. The agglomeration also occurred when the volume of tea waste extract increased. This phenomenon shows that the optimum volume of tea waste extract acts as reducing and capping agent is required to reduce agglomeration. The best photocatalytic degradation of 2,4-DCP was achieved using TiO₂-1 (85%) compared with TiO₂-3 (80%), TiO₂-5 (77%) and P25 (71%). The results reflect the decrease value of the bandgap and crystallite size with increasing surface area plays an important role in TiO₂ nanoparticles as photocatalyst.

ACKNOWLEDGEMENTS

The authors are grateful for the financial support by Universiti Sains Malaysia (USM) for Bridging Grant (R501-LR-RND003-0000000912-0000).

REFERENCES

- [1] Shoneye, A., Sen Chang, J., Chong, M. N., & Tang, J. (2022). *Int. Mater. Rev.* 67(1), 47–64.
- [2] Lin, J.C.T., Sopajaree, K., Jitjanesuwan, T., & Lu, M. C. (2018). *Sep. Purif. Technol.* 191, 233-243.
- [3] Alshabib, M., & Onaizi, S. A. (2019). *Sep. Purif. Technol.* 219, 186-207.
- [4] Li, Z., & Yang, P. (2018, February). In *IOP Conf. Ser.: Earth Environ. Sci.* (Vol. 113, p. 012185). IOP Publishing.
- [5] Malik, P., Shankar, R., Malik, V., Sharma, N., & Mukherjee, T. K. (2014). *J. Nanopart.* 2014.
- [6] Mukunthan, K. S., & Balaji, S. (2012). *Int. J. Green Nanotechnol.: Biomed.* 4(2), 71–79.
- [7] Jeevanandam, J., Chan, Y. S., & Danquah, M. K. (2016). *ChemBioEng Rev.* 3(2), 55-67.
- [8] Ansari, A., Siddiqui, V. U., Rehman, W. U., Akram, K., Siddiqi, W. A., Alosaimi, A. M., Hussein, M. A., & Rafatullah, M. (2022). *Catalysts*, 12(2), 181.
- [9] Singh, S., Maurya, I. C., Tiwari, A., Srivastava, P., & Bahadur, L. (2022). *Surf. Interfaces*, 28, 101652.
- [10] Mutalib, A.A.A., Jaafar, N.F. and Miskam, M., 2023. *Chem. Eng. Res. Des.*, 198, 105-120.
- [11] Kim, M. G., Kang, J. M., Lee, J. E., Kim, K. S., Kim, K. H., Cho, M., & Lee, S. G. (2021). *ACS Omega*, 6(16), 10668-10678.
- [12] Casino, S., Di Lupo, F., Francia, C., Tuel, A., Bodoardo, S., & Gerbaldi, C. (2014). *J. Alloys Compd.* 594, 114-121.
- [13] Shen, X.S., Wang, G.Z., Hong, X. and Zhu, W. (2009). *Phys. Chem. Chem. Phys.*, 11(34), 7450-7454.
- [14] Jaafar, N. F., Jalil, A. A., & Triwahyono, S. (2017). *Appl. Surf. Sci.* 392, 1068-1077.
- [15] Aravind, M., Amalanathan, M., & Mary, M. S. M. (2021). *SN Appl. Sci.* 3, 1-10.
- [16] Nabi, G., Ain, Q., Tahir, M. B., Riaz, K. N., Rafique, M., Hussain, S., Raza, W., & Aslam, I. (2022). *Int. J. Environ. Anal. Chem.* 102(2), 434–442.
- [17] Sushma, N. J., Mahitha, B., Mallikarjuna, K., & Raju, B. D. P. (2016). *Appl. Phys. A*, 122, 1-10.
- [18] Sibiya, P. N., & Moloto, M. J. (2016). *Asian J. Chem.* 28(6), 1315–1320.
- [19] Ahmed, K. K., Hussen, S. A., & Aziz, S. B. (2022). *Arab. J. Chem.* 15(7), 103913.
- [20] Saikumari, N., Preethi, T., Abarna, B., & Rajarajeswari, G. R. (2019). *J. Mater. Sci.: Mater. Electron.* 30, 68206831.

Biocomposite Material Using Sugarcane Bagasse and Modified Starch for Potential Packaging in Agroindustry

Visharavidev Palanisamy¹, Abd Halim Md Ali*^{1,2}, Pramila Tamunaidu^{1,2}, Muhammad Bukhari Rosly², Nurhamieza Md Huzir², Azlan Nur Rasyid Amin², Muhammad Hazwan Hamzah³

¹Department of Chemical and Environmental Engineering, Malaysia-Japan International Institute of Technology (MJIT), Universiti Teknologi Malaysia, Jalan Sultan Yahya Petra, Kampung Datuk Keramat, 54100 Kuala Lumpur, Wilayah Persekutuan Kuala Lumpur, Malaysia

²Malaysia-Japan Advanced Research Centre (MJARC), Universiti Teknologi Malaysia Kampus Pagoh, Hub Pendidikan Tinggi Pagoh, 84600, Pagoh, Johor, Malaysia

³Department of Biological and Agricultural Engineering, Faculty of Engineering, Universiti Putra Malaysia, 43400 UPM, Serdang, Selangor, Malaysia

*Corresponding Author: abd.halim@utm.my

Article history:

Received 08 August 2024

Accepted 26 September 2024

GRAPHICAL ABSTRACT



ABSTRACT

The widespread use of petroleum-based plastics in packaging has raised significant environmental concerns due to their non-biodegradability and detrimental ecological impacts. This study explores the development of an eco-friendly biocomposite material using sugarcane bagasse and cassava starch as potential alternatives for agro-industry packaging. The research objectives include characterizing the morphological properties of modified and unmodified sugarcane bagasse, analysing the thermal and physical properties of the resultant biocomposite, and evaluating its potential as a sustainable packaging material. A set of samples experiment were investigated using a constant ratio of distilled water to cassava starch which is 3:1 and 5 different ratios of acetic acid to bagasse. The morphological properties of biocomposite material which are sugarcane bagasse and cassava starch were examined using a Field-Emission Scanning Electron Microscope and Fourier Transmission Infrared Spectroscopy. Thermogravimetric Analysis (TGA) and Tensile strength were used to analyse thermal and physical property. Subsequently, the assessment of environmental friendliness was conducted by biodegradability testing. The results indicate that the most optimal biofilm, in terms of flexibility, thermal stability, and decomposition speed, was achieved with a ratio of (2:1) and (3:1) of acetic acid to bagasse. The results obtained suggest that sugarcane bagasse, when combined with cassava starch, can serve as an effective, biodegradable packaging material, potentially mitigating the environmental impact of conventional plastics in the agro-industry.

Keywords: biocomposite, biodegradable packing, thermal stability, sugarcane bagasse and cassava starch

© 2024 Faculty of Chemical and Engineering, UTM. All rights reserved
| eISSN 0128-2581 |

1. INTRODUCTION

The worldwide population depends on the agro industry to supply packaging material and other agricultural items. Most packaging materials produced were made used conventional packaging. Nevertheless, the agro-industry employment of conventional packaging materials offers several environmental challenges, such as waste and contamination. To tackle these difficulties and assured the agro-industry long-term development, sustainable packaging was essential [1]. Packaging materials that were sustainable, recyclable, biodegradable, and kind to the environment. Natural fibres and biodegradable polymers were combined to generate bio composite materials, which

provided a feasible solution for traditional packaging materials [2].

A typical plastic packaging item was the manufacture of biocomposite materials for packaging that used modified starch and sugarcane bagasse. They were constructed of natural fibres and biodegradable polymers. Biocomposite materials gave a more environmentally friendly and sustainable solution for packaging than conventional packaging materials [3]. Biocomposite materials were an innovative class of materials developed through combining natural fibres or particles with a matrix. By utilising their inherent durability and ecologically advantageous features of natural resources, these materials may construct composites with exceptional mechanical attributes. Moreover, there were natural resources that been employed

as biocomposite material such as wheat straw-based composites, rice husk composites and kenaf fibre composites. Along with that flow of natural resources the utilisation of sugarcane bagasse and modified starch was a vital component in the production of bio composite materials was the main aim of this work [4].

Considering this, sugarcane bagasse was a copious agro-industrial waste product that had been explored for employment in biocomposite materials designed for packaging applications due to its abundance as a resource, non-toxic, lightweight, ecological acceptable and a low cost by-product making it economically advantageous for large-scale production [5]. Modified starch, on the other hand, was a biodegradable polymer that may be manufactured from starch, a renewable resource industry [6]. Characterization procedures for biocomposite materials are critical in selecting optimal biomaterials for specific applications, emphasising its importance in innovative packaging solutions [7]. Overall, the exploitation of biocomposite materials in packaging corresponds with the increased consumer and industry desired for greener, more sustainable packaging choices, makes it a significant area of research and development in the agroindustry and packaging sectors [8].

2. EXPERIMENTS

2.1 Preparation of sample

The sugarcane bagasse was properly cleansed and grinded into little pieces before the drying process began. The sugarcane bagasse was then dried in an oven at 105°C for 24 hours to eliminate the moisture content and water. After the drying process, the sugarcane bagasse was grinded using a grinder to put it into powder form. Next, the sugarcane bagasse powder was sieved into 250 microns.

Cassava starch was sourced from a nearby store. For biofilm formulation, a constant ratio of 60 ml distilled water to 30 grams starch, along with 3 ml glycerol, was used. Samples with different ratios of acetic acid to bagasse (Table 1) were mixed in a beaker and heated on a hot plate with a magnetic stirrer at 85°C for 25 minutes until gelatinized. The thick solution was then poured onto a petri dish and left to dry.

Table 1. Samples with different ratios

Sample	Ratio	Acetic Acid (ml)	Bagasse (gram)	Glycerol (ml)
A	1:1	1	1	3
B	1:2	1	2	3
C	2:1	2	1	3
D	3:1	3	1	3
E	1:3	1	3	3

2.2 Morphological analysis of sugarcane bagasse and cassava starch

2.2.1. Field Emission Scanning Electron Microscope (FESEM)

The surface morphology of the biocomposite material was determined by Field Emission Scanning Electron Microscopy (JOEL-7800F Prime). The biocomposite material of sugarcane bagasse and cassava starch was placed in a holder before being inserted into the Field Emission Scanning Electron Microscopy to examine the sample's shape, size, and relative particle sizes. The surface morphology was examined at various magnifications during the analysis.

2.2.2. Fourier Transform Infra-Red (FTIR) Analysis

Fourier transform infrared spectroscopy is an important analytical tool for determining the presence of functional groups associated with the adsorbent. The annotated spectrum of FTIR show the wavelength of light that is absorbed, indicating the chemical bond in the AC. The surface functional groups of the bagasse and cassava starch were identified via FTIR analysis using an FTIR spectroscope, where spectra were obtained from 4000 to 650 cm^{-1} .

2.3 Thermal and physical property analysis

2.3.1 Thermogravimetric Analysis (TGA)

Thermogravimetric Analysis (TGA) was a potent method for evaluating a material's heat-related properties. It offered important details regarding the material's thermal stability and breakdown characteristics. The TGA curve's shoulders or peaks could point to certain thermal phenomena. The typical temperatures of constituents, such as cellulose, hemicellulose, or starch, could be utilized to determine their state of decomposition.

2.3.2 Universal Testing Machine (UTM)

The most significant mechanical characteristics of the bioplastic packaging material were its tensile strength and elongation at break, which were assessed using the UTM. Thus, it was favoured to describe the prepared biofilms in terms of their tensile strength and elongation at break. Tensile strength was described as the strength of material in terms of force per unit area of cross section while applying force in a straight direction.

2.2.4 Evaluation of Eco-Friendliness

Biodegradability testing was a crucial aspect of assessing the environmental impact of sugarcane bagasse-based packaging. The goal was to evaluate how well the material broke down into natural elements under different environmental conditions, particularly simulating scenarios like soil burial. 5 samples were prepared and exposed to identical soil conditions, with a uniform depth of 10 cm, and maintained at a constant ambient temperature of 27°C. This

experiment was conducted over a period of 7 days to assess the rate of degradation of different bioplastics.

3. RESULTS AND DISCUSSION

3.1 FTIR Characterization

Figure 1 shows the FTIR spectra of bagasse and cassava starch feature distinct absorption bands that reveal the chemical structure of starch molecules. Both materials show similar peaks, with a prominent peak at 3300 cm^{-1} indicating O-H stretching vibrations, suggestive of hydroxyl groups within the starch molecules [9]. An absorption band between 2000 to 1500 cm^{-1} corresponds to C=O stretching vibrations, typically found in esterified starches [10]. Additionally, a peak at 1000 cm^{-1} signifies the anhydro glucose ring O-C stretch, a trait of cassava starch.

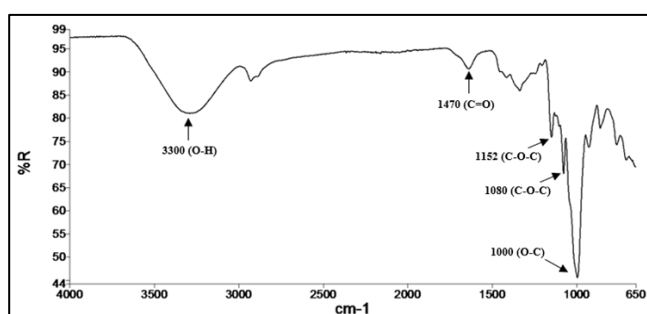


Fig. 1. FTIR of spectrum sugarcane bagasse and starch

Figure 2 shows the combined spectrum of sugarcane bagasse, starch, and glycerol includes peaks for cellulose at 1160 cm^{-1} , hemicellulose at 1740 cm^{-1} , and lignin between 1500 - 1600 cm^{-1} [11]. Cassava starch shows peaks for O-H stretching at 3300 cm^{-1} , C=O stretching around 1740 cm^{-1} , and C-O stretching at 1080 cm^{-1} . Glycerol's spectrum includes O-H stretching between 3200 - 3600 cm^{-1} , C-H stretching at 2900 cm^{-1} , and C-O stretching between 1100 - 1300 cm^{-1} [12].

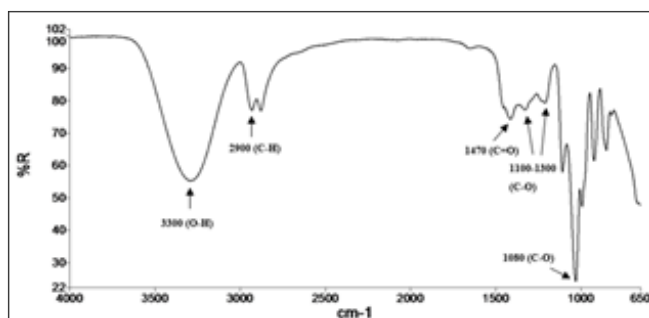


Fig. 2. FTIR spectrum of sugarcane bagasse, starch, glycerol

3.2 Field Emission Scanning Electron Microscope (FESEM)

For morphology analysis, FESEM images of unmodified and modified sugarcane bagasse were obtained as shown in Fig. 3. The smooth surfaces of unmodified sugarcane bagasse were observed due to the presence of hemicelluloses and lignin (Fig. 3A) [11]. After modification, a rough surface was observed signifying the elimination of hemicelluloses and lignin from sugarcane bagasse (Fig. 3B). The FESEM image reveals that the modified sugarcane bagasse is well-bound with starch, acetic acid and glycerol, which is consistent with the FTIR results.

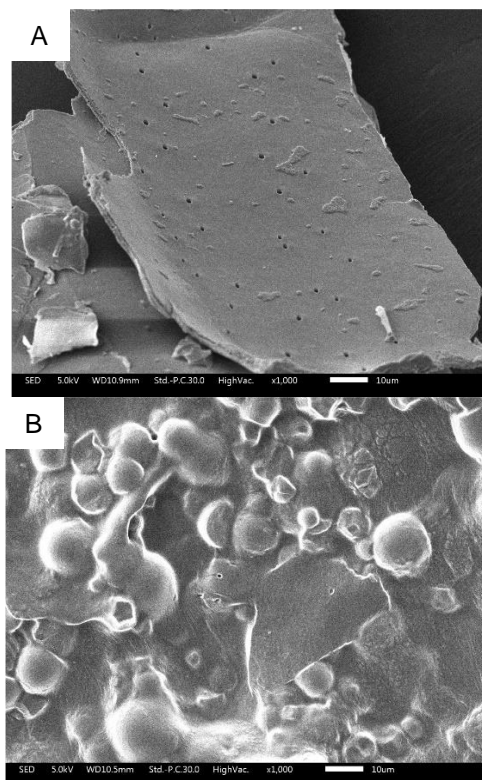


Fig. 3. FESEM images of (A) unmodified sugarcane bagasse and (B) modified sugarcane bagasse at $\times 1000$ magnification:

3.3 Tensile Strength and Elongation at break

To obtain strength test results, three sets of samples were prepared, each with five samples and varying ratios. The constant ratio used was 3 parts distilled water to 1 part cassava starch (60 ml water to 30 grams starch) along with a constant amount of glycerol. Among the three sets, the best sample was chosen based on the bioplastic thickness. Figure 4 shows the Force (N) vs Displacement (mm) results for bagasse and cassava starch packaging material tested at 10 mm/min at room temperature. The slope before the maximum point is the elastic slope, indicating the range in which the material can return to its original dimensions after unloading. The slope after the maximum point is the fracture slope, where the material does not return to its original dimensions once the load is removed [13]. Sample C, with a 2:1 ratio, exhibited the highest applied force of 17.9 N and a

thickness of 0.94 mm, indicating its superiority over the other samples.

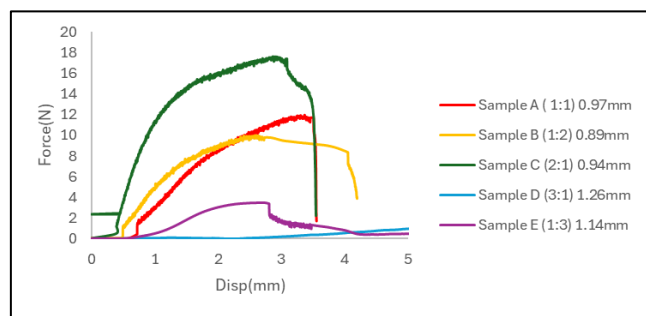


Fig. 4. Tensile strength of all the sample

3.4 Thermogravimetric Analysis

Figure 5 illustrates the thermal behaviour of five samples, showing a consistent pattern of gradual mass loss in distinct phases, as indicated by the TGA curves. The initial weight decreases between 80-150°C is due to the evaporation of water and volatile substances, known as the drying stage. The significant weight reduction occurs in the second phase, with temperatures ranging from 197-400°C for sample A (1:1), 193-390°C for sample B (1:2), 195-413°C for sample C (2:1), 220-415°C for sample D (3:1), and 200-398°C for sample E (1:3), primarily due to pyrolysis. Any further weight loss beyond 500°C is attributed to the decomposition of remaining carbonaceous materials.

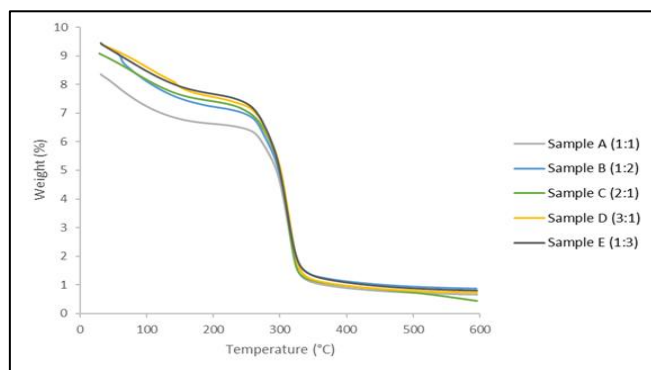


Fig. 5. Thermogravimetric Analysis

3.5 Derivative Thermogravimetric Analysis

Figure 6 shows prominent DTG peaks at 312.73°C, 311.99°C, 312.90°C, 313.46°C, and 310.33°C for samples A (1:1), B (1:2), C (2:1), D (3:1), and E (1:3), respectively, indicating the temperatures of maximal breakdown. Comparing the TGA and DTG curves of the five biofilm samples reveals that the temperatures for maximum decomposition rate (DTG) and thermal stability (TGA) do not follow a consistent pattern due to varying acetic acid to sugarcane bagasse ratios. Sample D, with a 3:1 ratio, shows the highest DTG value of 313.46°C and TGA values ranging

from 220-415°C. Figures 5 and 6 suggest that sample D is more thermally stable than the other samples. However, while the high degree of acetic acid enhances thermal stability, it may limit flexibility and further weaken mechanical strength, which is consistent with the tensile strength results shown in Fig. 4 [14].

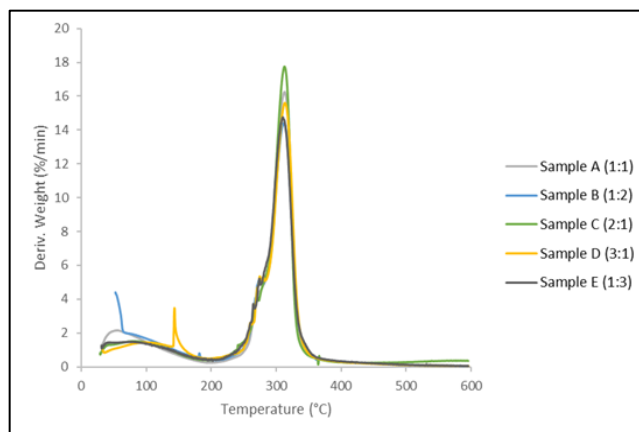


Fig. 6. Derivative thermogravimetric analysis of all the sample

3.6 Biodegradability Analysis

Figure 7 shows the soil burial process was used to assess the biodegradability of various bioplastics and significant degradation was noted by day 2, with sample A degrading 11.37%, sample B 2%, sample C 2.12%, sample D 1.74%, and sample E 1.13%.

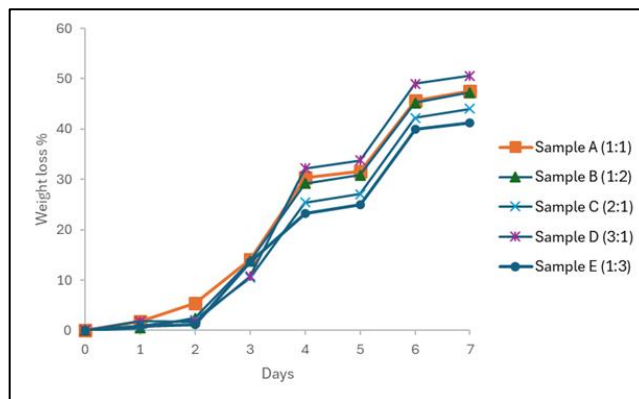


Fig. 7. Biodegradability analysis of all the sample

By day 4, sample A degraded by 30.43%, while samples B, C, D, and E degraded by 29.20%, 25.45%, 32.17%, and 23.31%, respectively. On the 7th day, weight loss ranged from 41% to 50%, with sample D showing the highest weight loss at 50%. These results indicate that sample D, with a 3:1 ratio of acetic acid to bagasse, degraded more rapidly than the other samples.

4. CONCLUSION

This work effectively created and examined biocomposite materials by using sugarcane bagasse and modified starch for prospective packaging uses in the agroindustry. The structural changes between modified and unmodified bagasse were observed by morphological characterization using FTIR and FESEM. Thermal and physical property study, such as Thermogravimetric study (TGA) indicates that an acetic acid to bagasse ratio of 3:1 is more thermally stable compared to the other samples and Universal Testing Machine (UTM), indicated that an acetic acid to bagasse ratio of 2:1 had the highest mechanical strength. The biodegradability testing has verified the environmentally favourable characteristics of the biocomposite. In summary, the combination of sugarcane bagasse and modified starch has great potential as a sustainable and efficient packaging material in the agricultural business.

REFERENCES

- [1] Aeschelmann, F., & Carus, M. (2015). *Industrial Biotechnology*, **11**(3), 154–159. <https://doi.org/10.1089/ind.2015.28999.fae>.
- [2] Jiménez, A., & Ruseckaite, R. A. (2012). *Green Energy and Technology* (pp. 393–408). https://doi.org/10.1007/978-1-4471-4108-2_15.
- [3] Amaraweera, S. M., Gunathilake, C., Gunawardene, O. H. P., Fernando, N. M. L., Wanninayaka, D. B., Dassanayake, R. S., Rajapaksha, S. M., Manamperi, A., Fernando, C. a. N., Kulatunga, A. K., & Manipura, A. (2021). *Molecules*, **26**(22), 6880. <https://doi.org/10.3390/molecules26226880>.
- [4] A.Balaji, B. Karthikeyan and C. Sundar Rajet. (2015). *Int. J. ChemTech Res.*, **07**(01), 223-233.
- [5] Reshmy, R., Thomas, D., Philip, E. *et al. Rev Environ Sci Biotechnol.* **20**, 167–187 (2021). <https://doi.org/10.1007/s11157-021-09565-1>.
- [6] *Biocomposites*. (n.d.). Retrieved March 21, 2024, from <https://www.greendotbioplastics.com>.
- [7] Compart, J., Singh, A., Fettke, J., & Apriyanto, A. (2023). *Polymers*, **15**(16), 3491. <https://doi.org/10.3390/polym15163491>.
- [8] Cristofoli NL, Lima AR, Tchoukouang RDN, Quintino AC, Vieira MC. (2023). *Sustainability*; **15**(7):6153. <https://doi.org/10.3390/su15076153>.
- [9] Christensen, P.A., Ali, A.H.B.M., Mashhadani, Z.T.A.W. *et al.* (2018). *Plasma Chem Plasma Process* **38**, 461–484. <https://doi.org/10.1007/s11090-018-9889-z>
- [10] Christensen, P.A., Ali, A.H.B.M., Mashhadani, Z.T.A.W. *et al.* (2018). *Plasma Chem Plasma Process*. **38**, 293–310. <https://doi.org/10.1007/s11090-018-9874-6>
- [11] Hamzah, M.H., Ibrahim, S.K., Nor, M.Z.M. *et al.* (2023). *Food Measure* **17**, 3732–3744). <https://doi.org/10.1007/s11694-023-01903-x>.
- [12] Christensen, P.A., Mashhadani, Z.T.A.W., Md Ali, A.H.B.: *Phys. Chem. Chem. Phys.* **20**, 9053–9062 (2018). <https://doi.org/10.1039/c7cp07829c>
- [13] A. Muhammad, A. R. Rashidi, A. Roslan, S. A. Idris; *AIP Conf. Proc.* 26 September 2017; **1885** (1): 020230. <https://doi.org/10.1063/1.5002424>
- [14] Boey, J.Y.; Lee, C.K.; Tay, G.S. (2022). *Polymers*, **14**, 3737. <https://doi.org/10.3390/polym14183737>

Evaluation of the Glass Transition Temperature and Intermolecular Interaction of Poly(ethylene oxide) with Addition of Lithium Perchlorate or/and Titanium Dioxide

S.N.H.M. Yusoff^{1,*}, N.F.A. Zainal²

¹Faculty of Applied Sciences, Universiti Teknologi MARA Cawangan Johor Kampus Pasir Gudang, 81750 Masai, Johor, Malaysia.

²Centre of Foundation Studies, Universiti Teknologi MARA, Cawangan Selangor Kampus Dengkil, 43800 Dengkil, Selangor, Malaysia

*Corresponding author: sitiinorhafiza@uitm.edu.my

Article history:

Received 01 September 2024

Accepted 30 October 2024

ABSTRACT

The high crystallinity of poly(ethylene oxide) (PEO) has urged the need for adding salt or nanofiller to explore the electrochemical performance of solid polymer electrolytes (SPEs). The effect of the glass transition temperature (T_g) and intermolecular interaction of PEO upon the addition of salt or nanofiller has become a debatable topic due to the lack of understanding of the role of salt or nanofiller in PEO. Hence, the evaluation of the T_g and intermolecular interaction of PEO with the addition of lithium perchlorate (LiClO_4) salt or/and titanium dioxide (TiO_2) nanofiller is presented and discussed. The solid polymer electrolytes with the addition of nanofiller are prepared by solution casting technique. The optimum composition of PEO and LiClO_4 salt is used as the host matrix and TiO_2 as the nanofiller. The T_g and intermolecular interaction of the polymer-based electrolytes have been studied by Differential Scanning Calorimeter (DSC) and Fourier Transform Infrared spectroscopy (FTIR), respectively. PEO- LiClO_4 serves as the classical model of polymer-salt systems with good polymer-salt molecular interaction at low salt concentrations ($W_s \leq 0.107$) whereas TiO_2 without any surface treatment when added to PEO, serves as a classical model of polymer-nanofiller systems with weak polymer-nanofiller molecular interaction. Results have shown that LiClO_4 salt has a notable effect on the T_g and intermolecular interaction of PEO. Whereas, TiO_2 does not provide a substantial effect on the T_g and intermolecular interaction of PEO-based polymer electrolytes. This work provides a better understanding and knowledge of the effect of the addition of salt or/and nanofiller in the T_g and intermolecular interaction of the PEO systems.

Keywords: intermolecular interaction, glass transition temperature (T_g), poly(ethylene oxide), lithium perchlorate, titanium dioxide

© 2024 Faculty of Chemical and Engineering, UTM. All rights reserved

| eISSN 0128-2581 |

1. INTRODUCTION

Solid polymer electrolytes (SPE) have garnered significant interest in recent decades owing to their potential applications in solid-state batteries, fuel cells, supercapacitors, sensors and etc. [1–9]. SPE is prepared by dissolving the alkali metal salt in a polymer host [10–12]. These electrolytes provide several appealing benefits compared to their liquid counterparts, including leakage-free, safe, lightweight, and easy to synthesize in desirable thickness and area [2,13]. PEO-based solid polymer electrolyte is extensively studied due to its lower lattice energy [14], high solvating power for alkali metal salts [15], good electrochemical stability [16], and appropriate structure for facilitating rapid ion transport [17]. PEO contains Lewis base ether oxygen, which coordinates with the cations and thus helps to dissolve the inorganic salts

[1,17,18]. The main drawback of PEO-based solid polymer electrolyte is its high crystalline phase below the melting temperature which renders it unsuitable for application in batteries or other practical electrochemical devices. It has been revealed that the neat semicrystalline PEO has ~70% of the crystalline phase [19,20].

To address this issue, researchers have explored various strategies to enhance the overall performance of PEO-based electrolytes. These strategies include the incorporation of plasticizers to disrupt the crystalline structure [21,22], the use of nanofillers to enhance ion transport pathways [23,24], and the optimization of polymer-salt interactions. Furthermore, advances in material processing techniques and composite formulations are being investigated to reduce the crystallinity and improve the electrochemical properties of PEO-based electrolytes. Ongoing research aims to balance the mechanical stability,

ionic conductivity, and thermal stability of these materials, paving the way for their broader application in next-generation energy storage and conversion technologies.

For concept-proof, a lithium salt is chosen to be added to the PEO matrix for the application of SPE due to the high solvating property of PEO with the inorganic salt [11,25]. However, due to the high crystallinity of PEO, this may limit the application of the binary mixture of PEO with a salt as SPE [26]. The dissolution of salt only occurs in the amorphous region of the polymer matrix, where it plays the percolation pathway for the conductivity of dipolar entities of salt and PEO [27]. Meanwhile, inert nanofiller titanium dioxide (TiO₂) may offer excellent characteristics for the improvement of lithium-ion batteries [22,28,29]. However, inconsistent implications were deduced from the previous studies on how the nanofiller affects the properties and enhances the conductivity of the SPEs [30,31]. To date, the correlation of T_g-intermolecular interaction is crucial for regulating the performance of SPEs especially on the molecular interaction between the active surface of the nanofiller and the polymer chains, for which this attributing factor may be oversimplified [32,33].

Since there are limited reports on the effects of the addition of nanofiller into the SPEs that may lead to an enhancement in their performance for applications in batteries and other electrochemical devices, this work will explore the relationship between thermal properties and intermolecular interactions when PEO is added with salt and/or nanofillers. Differential Scanning Calorimeter (DSC) and Fourier Transform Infrared spectroscopy (FTIR) technique is employed to study the glass transition temperature (T_g) and to elucidate specific polymer-salt, polymer-nanofiller and polymer-salt-nanofiller intermolecular interaction of PEO with the addition of salt or/and nanofiller, respectively [34,35]. This will include a detailed discussion on the shifting of wavenumbers, changes in band shapes and intensities, and alterations in other band properties. The T_g of PEO and its molecular interactions with salts and nanofillers play crucial roles in determining the performance of PEO-based solid polymer electrolytes. By understanding and manipulating these factors, researchers can design electrolytes with optimized properties for various applications in energy storage and conversion technologies.

2. EXPERIMENTAL SECTION

2.1 Materials

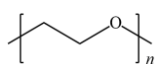
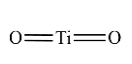
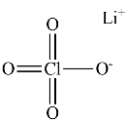
Three systems, *i.e.*, (1) polymer-salt, (2) polymer-nanofiller and (3) polymer-salt-nanofiller systems were studied in this work. PEO as the polymer host, LiClO₄ as the salt, and TiO₂ as the nanofiller were employed in this work. In this work, the rutile form of TiO₂ with a particle size of < 100 nm (99.5% trace metal basis) was selected due to its structural stability at various temperatures, high chemical stability, excellent optical transparency [36] and more surface active than other fillers [2,37] which offers various

fields of potential applications for example photocatalysis [38], pharmaceuticals [39], electronic devices [40], *etc.* Therefore, TiO₂ was chosen as the conceptual model for this study in order to explore the effect of incorporating TiO₂ into a polymeric system. This will facilitate a more comprehensive understanding of the applicability of TiO₂ to be used as a nanofiller in polymeric systems.

PEO was purified by dissolution in chloroform (CHCl₃) (Merck, Darmstadt, Germany) and precipitation in *n*-hexane (Merck, Darmstadt, Germany) before the addition of salt or nanofiller. The salt and nanofiller were dried at 120 °C for at least 24 h prior to sample preparation. The characteristics of the polymer, salt, and nanofiller used in this work are tabulated in

Table 1.

Table 1. Characteristics of materials used in this work

Constituent	PEO	TiO ₂	LiClO ₄
M_n^a (g mol ⁻¹)	300,000	-	-
M_w^b (g mol ⁻¹)	-	79.87	106.4
T_m (°C)	65 ^c	-	236 ^d
T_g^e (°C)	-53	-	-
Molecular structure			
Supplier	Sigma-Aldrich (St. Louis, MO, USA)	Sigma Aldrich Chemical Co. (USA)	Acros Organics Co, Geel, Antwerp, Belgium

^aViscosity-average molar mass estimated by the supplier;

^bMolar mass calculated by the supplier; ^cMelting temperature adapted from ref [19]; ^dMelting temperature adapted from ref [41]; ^eGlass transition temperature estimated from DSC as determined in this work

2.2 Sample Preparation

A solution-casting technique was used to prepare the free-standing polymer-salt, polymer-nanofiller and polymer-salt-nanofiller films. The PEO was added with different salt fraction (W_S) in the range of 0 to 0.17, or nanofiller fraction (W_F) in the range of 0 to 0.065 for preparation of polymer-salt or polymer-nanofiller films, respectively. The equation to determine the mass fraction of salt and nanofiller is as follows

$$W_i = \frac{m_i}{m_{PEO} + m_i} \quad (1)$$

where quantity m_i and m_{PEO} represent the mass of component i and PEO, respectively. The component i can be noted as the salt or nanofiller used in this work. For polymer-salt systems, the PEO was dissolved in tetrahydrofuran (THF)

(Merck, Darmstadt, Germany) and was stirred for at least 24 h at 50 °C. The polymer-salt mixture was poured onto the Teflon dish and was left to dry without undergoing extra stirring. Unlike the polymer-salt mixture, the polymer-nanofiller system was dissolved in acetonitrile (ACN) (Merck, Darmstadt, Germany) and was stirred for at least 24 h at 50 °C. ACN was used to prepare the polymer-nanofiller solutions due to the higher polarity and interaction of ACN, which promotes better dispersion of a highly agglomerated TiO₂ filler in the polymer solution. Further stirring using T18D Ultra-Turrax homogenizer (IKA, Stauffer, Germany) for 15 min at a speed of 5000 rpm was done for the polymer-nanofiller mixture in order to reduce the agglomeration of the nanofiller. Meanwhile, for the preparation of polymer-salt-nanofiller systems, the composition of salt is fixed based on the optimum composition of salt obtained from the polymer-salt system (*i.e.*, $W_S = 0.107$) with increasing nanofiller fraction (W_F) in the range of 0 to 0.043. The range of composition of nanofiller before the agglomeration of nanofiller (*i.e.*, obtained from polymer-nanofiller systems). The polymer-salt-nanofiller system was dissolved in ACN and was stirred for at least 24 h at 50 °C and further stirred using homogenizer for another 15 min at a speed of 5000 rpm.

Then, the polymer-salt, polymer-nanofiller and polymer-salt-nanofiller mixture was poured slowly onto the Teflon dish and left to evaporate until a dried film was formed. After drying, all systems were heated at 80 °C under a nitrogen atmosphere for 30 min (to erase the thermal history during the sample preparation) before being further dried in a vacuum oven for 24 h at 25 °C. All samples were kept in desiccators before further characterization.

2.3. Instruments

2.3.1 Differential Scanning Calorimetry (DSC)

Thermal properties of polymer-salt, polymer-nanofiller and polymer-salt-nanofiller systems were studied using DSC TA Q200 (TA Instrument, New Castle, USA) equipped with RCS90 cooling system (TA Instrument, New Castle, USA). Before the analysis, calibration using indium and sapphire standards was done. Around 10 to 15 mg of the sample was used for each analysis. The sample was placed in a standard aluminium sample pan (*i.e.*, sealed hermetic pan) before starting the thermal procedure for DSC analysis. The sample was cooled to -90 °C and heated up to 80 °C at a rate of 10 °C min⁻¹. Nitrogen gas was purged throughout the analysis at a rate of 50 mL min⁻¹ to avoid the thermo-oxidative degradation of the sample in the DSC furnace. The quantity of T_g of the sample was extracted from the first heating cycle of DSC thermogram. The T_g was extrapolated at the mid-point of the change in heat capacity (ΔC_p) or by using Moynihan's method for a more precise estimation of T_g especially for the sample with the existence of relaxation endotherm in the glass transition[42–44]

2.3.2 Fourier Transform Infrared (FTIR)

The intermolecular interactions of the film samples with a thickness of 0.2 – 0.4 mm were examined by FTIR spectroscopy. The FTIR spectrum of each polymer-salt, polymer-nanofiller and polymer-salt-nanofiller systems were recorded using an attenuated total reflectance (ATR) accessory with a diamond crystal window on Nicolet iS10 FTIR (Thermo Scientific, Madison, Wisconsin, USA). The dried film was pressure-clamped to ensure that the film was in adequate contact with the ATR crystal. The spectra were collected in absorbance mode in the range of wavenumber 600 - 4000 cm⁻¹ by averaging 16 scans at a maximum resolution of 2 cm⁻¹ at 25 °C. The sample was analyzed at three locations with a minimum of six FTIR measurements to ensure that the FTIR analysis was based on a representative region of the polymer-salt, polymer-nanofiller and polymer-salt-nanofiller systems, respectively. The spectrum obtained was subjected to background subtraction and auto-baseline correction to attain the final spectrum.

3. RESULTS AND DISCUSSION

3.1 Glass Transition Temperature

T_g is one of the important properties of polymers, which describes the temperature at which the polymer chains start to move. Below T_g , the polymer chains are rigid and have very little mobility. The T_g is influenced by the molecular structure of polymers [45,46], molar mass [44,47], crystallinity and thermal history [48]. Lowering the T_g can increase the polymer chains' mobility and consequently increase the conductivity [49,50]. This is due to the enhanced flexibility of the polymer chains and faster segmental motion. Since the conductivity of SPEs at room temperature is still low, strategies have been conducted in an attempt to lower the T_g far below room temperature and enhance the conductivity.

Figure 1 shows the T_g of amorphous PEO for PEO-LiClO₄, PEO-TiO₂ and PEO-LiClO₄-TiO₂ systems. There is a linear increase in T_g with elevating salt content up to $W_S = 0.0909$ for the PEO-LiClO₄ systems but not in the PEO-TiO₂ and PEO-LiClO₄-TiO₂ systems. This shows that the salt has a significant effect on the amorphous region of the semicrystalline PEO than the nanofiller. In other words, the salt possesses better interaction with PEO than the nanofiller. One can see that the variation in T_g for the polymer-based nanofiller systems is insignificant as each T_g -nanofiller composition is within the percentage error. Besides, it is also well-known that the salt is more soluble in PEO, unlike the ceramic nanofiller, where phase separation takes place in the binary (or ternary) mixture, even with surface modification of the nanofiller [51–55]. This is because the ceramic nanofiller does not dissolve in the polymer.

It can be seen that PEO-LiClO₄ systems are only miscible up to a certain composition as the T_g increase linearly up to saturation point ($W_S > 0.107$), before it drops until reaching near the T_g of neat PEO (T_g^0), indicating the occurrence of phase separation in the amorphous region. In

other words, above the saturation point at $W_s > 0.107$, PEO-LiClO₄ systems undergo a phase separation forming the salt-rich and salt-poor phases. Salt-rich and salt-poor phases refer to the pure salt phase (salt precipitation due to excessive amount of salt in PEO) and the phase of highly diluted salt solution in the PEO, respectively. This phase can be observed from the micrograph from the polarized optical microscope (POM) that has been reported in previous work [20,56]. It is well noted that an increase in T_g elucidates the increase in rigidity of the polymer chain, which may also imply the interaction between the constituents in the mixture [57–59]. Hence, from the presented data, the increase in T_g observed in PEO-LiClO₄ systems implies the interaction between PEO and LiClO₄ salt. Consequently, it leads to a decrease in the degree of freedom of molecular chains of PEO with elevating salt fraction unlike the TiO₂ nanofiller, where little to no effect on the degree of freedom of PEO chains. This observation is absent for the PEO-TiO₂ and PEO-LiClO₄-TiO₂ systems which expresses the immiscibility of TiO₂ and PEO.

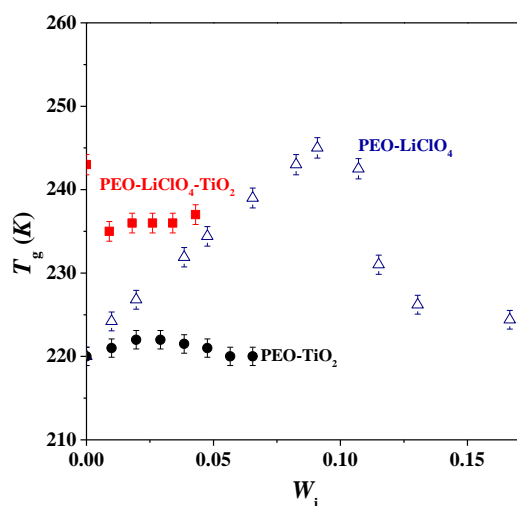


Figure 1. Glass transition temperature of amorphous PEO for (Δ) PEO-LiClO₄, (●) PEO-TiO₂ and (■) PEO-LiClO₄-TiO₂ systems. The error bar represents the standard deviation of the T_g values with an error of less than 3%.

The molecular dispersion of salt in the PEO might be possible due to the complex interaction of salt molecules and PEO segments but it is impossible for the PEO with incorporation of TiO₂ nanofillers. Molecular chains of PEO, as well as the TiO₂, behave like hard spheres to each other as they dislike each other, hence, phase separation takes place in the amorphous phase of PEO. The TiO₂ nanofiller agglomerates and forms micro-particles with an elevating mass fraction of TiO₂ that may lead to severe phase separation [19,20]. Thus, leads to the insignificant difference in T_g for the immiscible system as indicated by the constancy of T_g of PEO with increasing of nanofiller content for PEO-TiO₂ and PEO-LiClO₄-TiO₂ systems.

3.2 Intermolecular Interactions

FTIR is a powerful vibrational spectroscopic method that is widely used to study the intermolecular interactions between components of a polymer mixture [2,60,61]. FTIR is a useful characterization tool as it provides information on the complexation between salt and polymer, nanofiller and polymer, and salt, nanofiller and polymer systems. In general, the shifting in wavenumbers or/and the changes in the intensities of the characteristic absorption peaks of polymer complexes using FTIR give an insight into the interactions that occur between the components of the complex system which may allow one to elucidate the structure of the complex system.

The characteristics of the neat PEO, PEO-LiClO₄, PEO-TiO₂ and PEO-LiClO₄-TiO₂ systems were checked using FTIR. The FTIR analysis is discussed here to highlight the absorption bands of neat PEO, PEO-LiClO₄, PEO-TiO₂ and PEO-LiClO₄-TiO₂ systems. Therefore, the change in the IR absorption bands of PEO upon the addition of salt or nanofiller or salt and nanofiller can be highlighted. Figure 2 shows the full range of FTIR spectra (i.e., wavenumber range from 4000 to 650 cm⁻¹) of neat PEO, PEO-LiClO₄, PEO-TiO₂ and PEO-LiClO₄-TiO₂ systems. The assignment of characteristic IR bands of PEO is based on the previous work by other researchers are listed in Table 2. The characteristic of IR bands of neat PEO in this study is found to be substantially similar to the characteristic IR bands extracted from the literature.

The most important vibrational modes and wavenumbers exhibited by neat PEO are CH₂ bending [ν_s (CH₂)], CH₂ wagging [ω (CH₂)] and C–O–C stretching [ν (C–O–C)] modes. Generally, the characteristic ω (CH₂) mode of PEO shows a sharp doublet at 1360 and 1342 cm⁻¹ representing the crystalline phase of PEO. The centre peak of ν (C–O–C) mode appears as a triplet at 1095 cm⁻¹ that corresponds to the amorphous part of PEO, while the two shoulders represent the crystalline phase of PEO at 1145 and 1060 cm⁻¹, respectively [60].

With the addition of LiClO₄ (i.e., $W_s = 0.0099$) to the PEO matrix, the absorbance bands of PEO show a slight difference in peak wavenumber shifting as compared to the neat PEO. Meanwhile, with incorporation of TiO₂ (i.e., $W_f = 0.0099$) into the PEO matrix reveals that the FTIR spectrum of the PEO-TiO₂ system closely resembles that of the neat PEO except for a little change in the intensities of a few peaks which are peaks of the ν (C–O–C) modes. Besides, the FTIR spectra for PEO-LiClO₄-TiO₂ at $W_s = 0.107$, $W_f = 0.009$ show relatively fewer changes in the wavenumber and peak intensities of the vibrational bands of PEO-LiClO₄-TiO₂ with the addition of nanofiller as compared to PEO-TiO₂ systems. The vibrational modes of CH₂ stretching, CH₂ wagging and C–O–C stretching were shifted to higher wavenumbers. The shape of all CH₂ modes changed with decreased intensity.

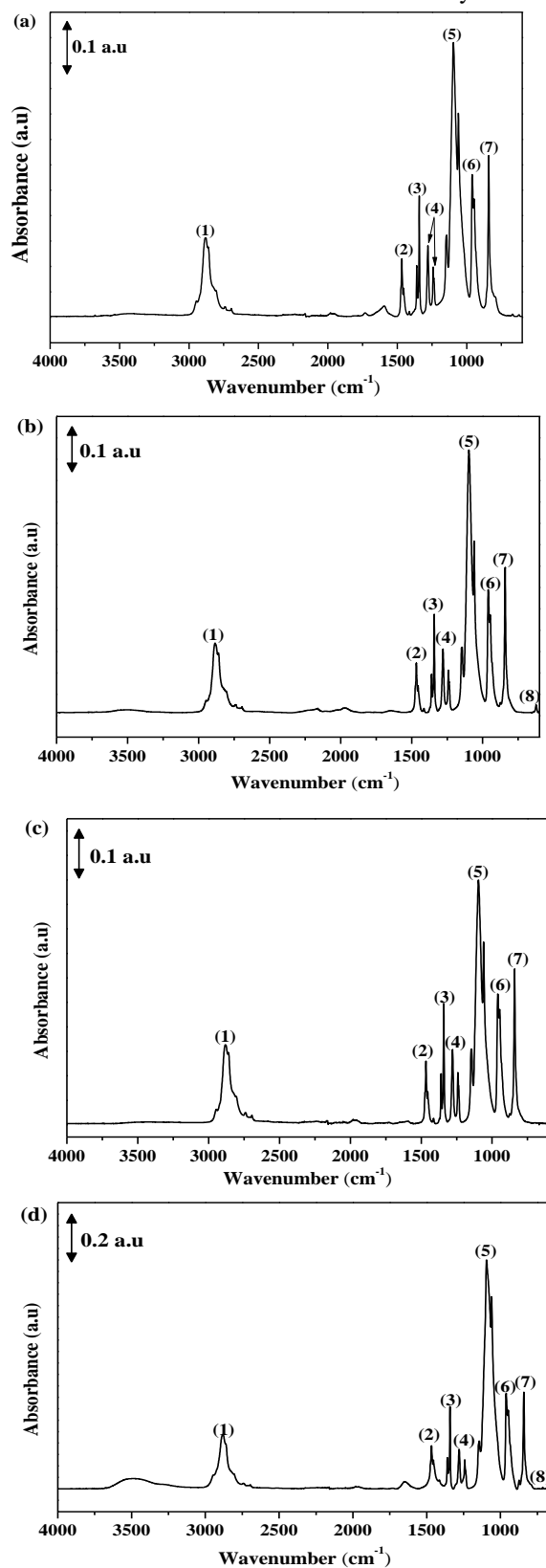


Figure 2. FTIR spectra of (a) neat PEO, (b) PEO-LiClO₄ at $W_S = 0.0099$, (c) PEO-TiO₂ at $W_F = 0.0099$ and (d) PEO-LiClO₄-TiO₂ systems at $W_S = 0.107$, $W_F = 0.009$, respectively.

Figure 3 (a) and (b) show the enlarged view of the absorption bands of CH₂ stretching and CH₂ wagging of PEO-LiClO₄ systems, respectively. The peak intensity at a wavenumber of 1342 and 2884 cm⁻¹ are reduced as the amount of the addition LiClO₄ increasing indicates that the addition of LiClO₄ disrupted the ordering of the polymer chains of PEO and increased the amorphous of PEO [69]. However, the wavenumbers of PEO-LiClO₄ systems at all salt compositions do not shift significantly.

Figure 3 (b) depicts two sharp absorption bands at 1360 and 1342 cm⁻¹ representing the crystalline phase of PEO [60,63–66]. There is no shifting of the wavenumber of the absorbance bands at 1342 cm⁻¹ with the addition of LiClO₄, but the absorbances of these bands reduce as the content of LiClO₄ in the PEO matrix increases, which indicates qualitatively proportionate to the lower content of the crystalline phase in the PEO [70].

Furthermore, another three important absorption IR bands of PEO are also observed to represent C-O-C stretching mode of the band [c.f.

Figure 3 (c)]. The middle peak of $\nu(\text{C-O-C})$ mode observed at 1095 cm⁻¹ corresponds to the amorphous phase of PEO, while the two shoulders representing the crystalline phase of PEO are observed at 1060 and 1148 cm⁻¹ [60,62–65]. There is a slight shifting of absorbance bands of $\nu(\text{C-O-C})$ mode of the amorphous phase of PEO to lower frequency (*i.e.*, from 1095 to 1078 cm⁻¹) and becomes broadened in shape. This is confirmed that there is the interaction between LiClO₄ with the amorphous phase of PEO. As for the shoulders, no clear shifting of the absorbance bands is observed. This is true since the LiClO₄ did not interact with the crystalline region of PEO [19,20]. However, the intensity of the absorbance peak becomes lower upon the addition of LiClO₄.

The band of 623 cm⁻¹ is assigned as the perchlorate “free” anion vibrations (ClO₄⁻) [27,35]. This band is frequently used to analyze ion-ion interactions in PEO-LiClO₄ systems [70]. The $\nu(\text{ClO}_4^-)$ mode of PEO in

Figure 3 (d) shows insignificant shifting in the wavenumber with ascending LiClO₄ content in the PEO matrix implying ions dissociation within the range of the salt content [27]. However, the intensity of the band increases with the increase of the salt content. This may suggest that there is an increment in the amount of free ClO₄⁻ anion or the dissociation of Li cation is also increased. Hence, it is confirmed by FTIR spectra that PEO-LiClO₄ systems have good polymer-salt intermolecular interaction at low salt content but weak polymer-salt intermolecular interaction at high salt content.

Figure 4 illustrates the FTIR spectra of $\omega(\text{CH}_2)$ and $\nu(\text{C-O-C})$ of PEO-TiO₂ systems. The composition of nanofiller is kept low (*i.e.*, $W_F \leq 0.0654$) because TiO₂ starts to agglomerate in the amorphous region of PEO and forms micro-size particles at high composition of nanofiller [19,20,40,71,72]. The doublet of $\omega(\text{CH}_2)$ that represents the crystalline phase of PEO remains unchanged in both position and intensity at all nanofiller compositions [c.f., Figure 4 (a)

and (b)]. This implies that the crystallinity of PEO has no or little interaction with the addition of nanofillers [19,73,74]. Normally, good molecular interactions lead to

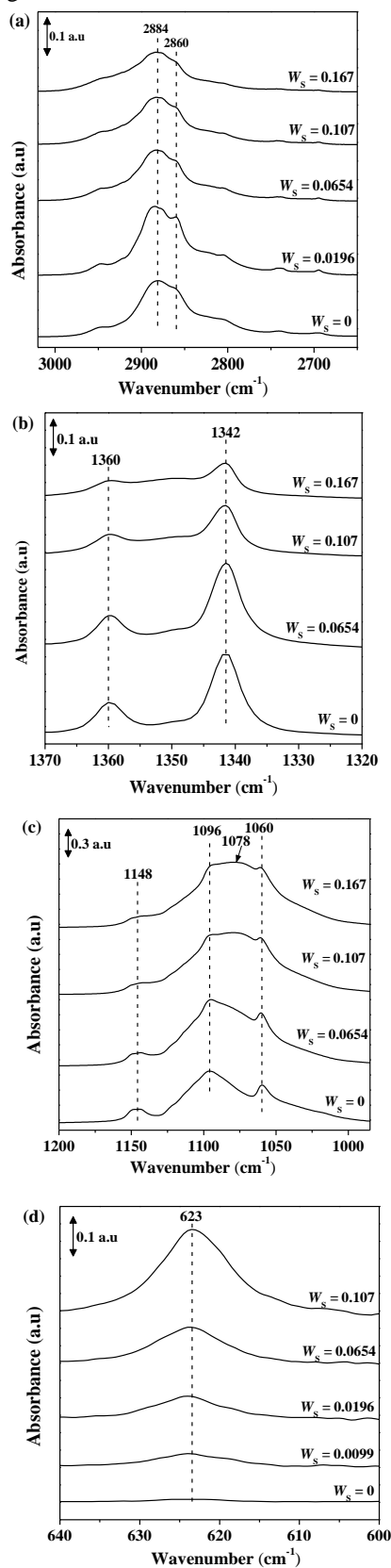


Figure 3. FTIR spectra of (a) CH₂ stretching, (b) CH₂ wagging, (c) C-O-C stretching and (d) ClO₄⁻ of PEO-LiClO₄ systems

largely modifying the shape of the bands and their peak positions [71]. In other words, the PEO matrix is not affected by the addition of TiO₂. However, it can be noted from the enlarged view presented in Figure 4 (c), there are no significant changes neither in intensity nor in positions of the triplet of absorbance bands of $\nu(\text{C-O-C})$ mode at 1060, 1096 and 1147 cm⁻¹ for PEO-TiO₂ systems even increasing the nanofiller content up to $W_F = 0.0654$. These results confirm that there are weak intermolecular interactions between the PEO functional group and TiO₂ in the PEO-nanofiller system because intermolecular interactions significantly alter the shape of the bands and their peak positions [71,75]. In this scenario, the presence of TiO₂ primarily functions as a physical confinement for PEO chains which potentially causes changes in their molecular arrangement and crystalline structures as reported by reference [61,71]. Hence, it is confirmed that the addition of TiO₂ without any surface treatment into the PEO matrix did not have substantial effects on the molecular interaction between PEO and nanofiller in PEO-TiO₂ systems. It serves as a classical model of polymer-nanofiller systems with weak polymer-nanofiller molecular interaction.

The enlarged view of a doublet of $\omega(\text{CH}_2)$ for PEO-LiClO₄-TiO₂ systems at a fixed amount of salt, $W_S = 0.107$ which represents CH₂ stretching and CH₂ wagging are depicted in Figure 5 (a) and (b), respectively. The peak intensity of a doublet of $\omega(\text{CH}_2)$ and their wavenumbers at all nanofiller compositions of PEO-LiClO₄-TiO₂ systems remain unchanged as the amount of TiO₂ increases indicating that the crystalline phase of PEO is unaffected with the addition of nanofiller. In addition, no difference is observed when the addition of TiO₂ as low as $W_F = 0.009$ in PEO-LiClO₄-TiO₂ systems for absorbance bands of $\nu(\text{C-O-C})$ mode where the peak intensity and the wavenumber (*i.e.*, 1094, 1059 and 1146 cm⁻¹) are insignificant changes. Normally, the interactions among PEO, LiClO₄ and TiO₂ are associated with the changes in intensity, shape and position of these stretching modes [70]. Hence, this observation may indicate weaker or no interaction of LiClO₄ and PEO after the addition of TiO₂. However, the loose boundary region may exist at the interface of TiO₂ and PEO. As a result, it may allow the attraction of charged entities to the loose boundary of TiO₂ which possibly helps in the facilitation of the charged entities at the interface of TiO₂ and PEO [76].

Moreover, the band of 623 cm⁻¹ shows an insignificant shift in the wavenumber with an ascending concentration of TiO₂ [*c.f.*, Figure 5 (d)]. This may suggest that there is no significant variation in the amount of free ClO₄⁻ anion or dissociation of Li cation when a small amount of TiO₂ is added. This is due to the charged entities may be attracted more to the loose interfacial region around the surface of TiO₂ [76], thus weakening the interaction of PEO and LiClO₄. Hence, it led to insignificant changes for the free anion and dissociated cation of the PEO-LiClO₄-TiO₂ ternary systems.

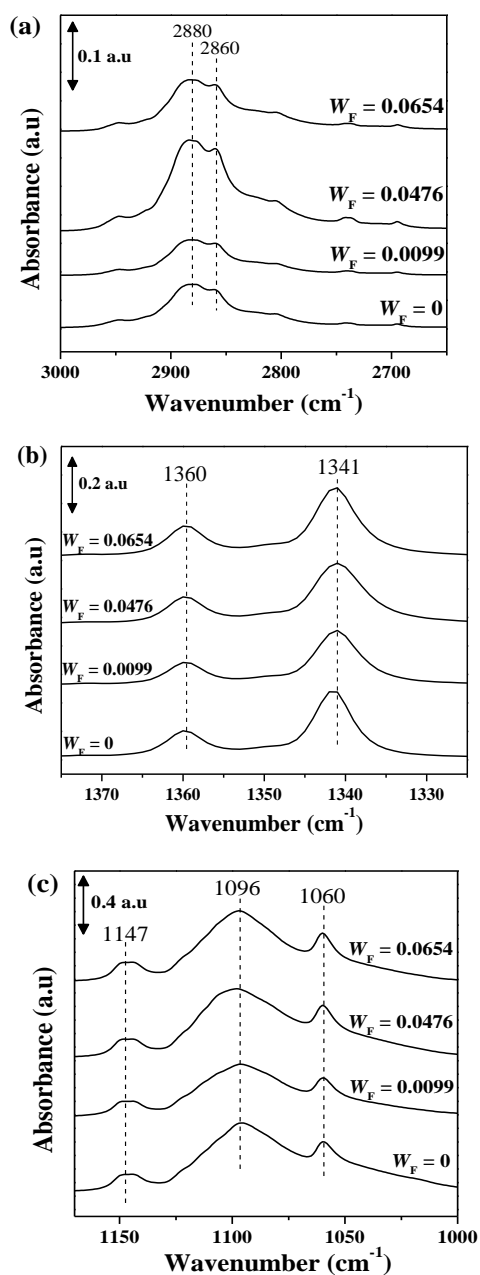


Figure 4. FTIR spectra of (a) CH₂ stretching, (b) CH₂ wagging and (c) C-O-C stretching of PEO-TiO₂ systems

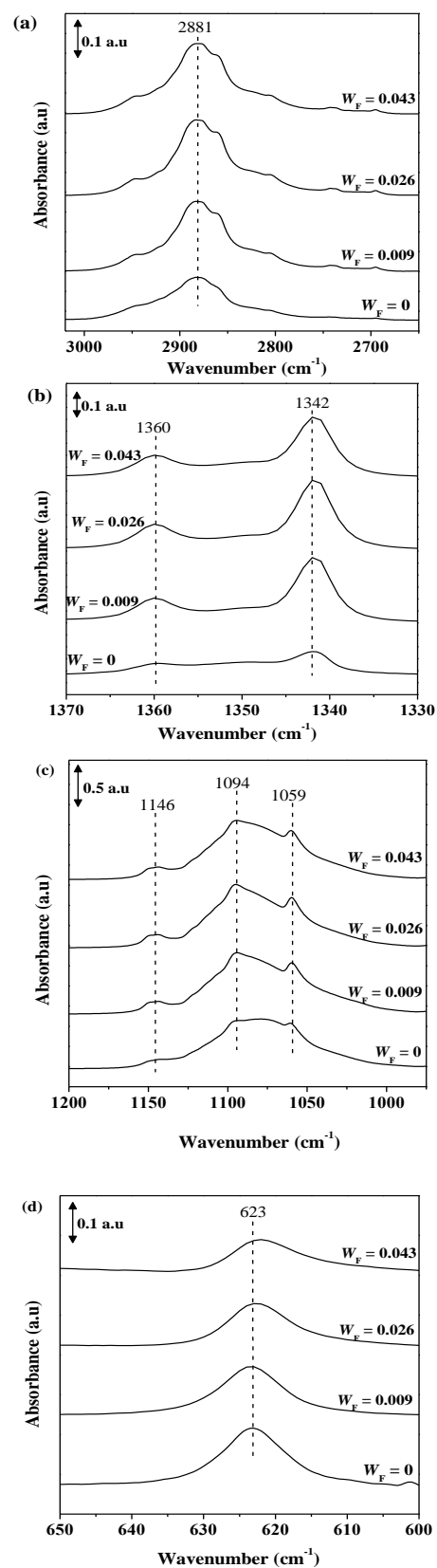


Figure 5. FTIR spectra of (a) CH₂ stretching, (b) CH₂ wagging, (c) C-O-C stretching and (d) ClO₄⁻ of PEO-LiClO₄-TiO₂ systems at fixed salt content, $W_S = 0.107$

Table 2. Characteristics IR bands for neat PEO, PEO-salt, PEO-nanofiller and PEO-salt-nanofiller systems

No	Assignment	Neat PEO		PEO-LiClO ₄ system (W _S = 0.0099)		PEO-TiO ₂ system (W _F = 0.0099)	PEO-LiClO ₄ - TiO ₂ system (W _S = 0.107, W _F = 0.009)
		Wavenumber (cm ⁻¹)	Refs.	Wavenumber (cm ⁻¹)	Refs.	Wavenumber (cm ⁻¹)	Wavenumber (cm ⁻¹)
(1)	CH ₂ stretching, ν_s (CH ₂)	2886	[60,62–64]	2884	[60,62–64]	2880	2881
(2)	CH ₂ scissoring, δ_{as} (CH ₂)	1466	[60,62–64]	1467	[60,62–65]	1466	1466
(3)	CH ₂ wagging doublet, ω (CH ₂)	1342, 1360	[60,63,64,66]	1342, 1360	[60,63–66]	1341, 1360	1342, 1360
(4)	CH ₂ twisting, ω (CH ₂)	1240, 1280	[35,60,63,64]	1240, 1279	[35,60,63–65]	1240, 1281	1240, 1281
(5)	Symmetric C-O-C stretching, ν (C-O-C)]	1060, 1095, 1145	[60,62–64]	1060, 1096, 1148	[60,62–65]	1060, 1096, 1147	1059, 1094, 1146
(6)	CH ₂ symmetric rocking, ρ_s (CH ₂)	962	[35,60,63,64]	961	[35,60,63–65]	961	962
(7)	CH ₂ asymmetric rocking, ρ_{as} (CH ₂)	842	[35,60,64,67]	841	[35,60,64,65,67]	841	842
(8)	ν (ClO ₄ ⁻)	n.a		623	[35,65,68]	n.a	623

4. CONCLUSION

This work focuses on the effect of the addition of salt or/and nanofiller on the T_g and intermolecular interactions of PEO-LiClO₄, PEO-TiO₂ and PEO-LiClO₄-TiO₂ systems. The values of T_g for the amorphous phase of PEO increased with ascending salt content before starting to decrease at a higher salt fraction, $W_S \geq 0.107$. The values of T_g for PEO-TiO₂ and PEO-LiClO₄-TiO₂ systems do not change significantly with an increment of nanofiller fraction. This indicates that there is little or no effect of the addition of TiO₂ to the PEO and PEO-salt systems.

Besides, the FTIR study revealed there is a slight shifting of absorbance bands of asymmetric and symmetric C-O-C stretching mode of the amorphous phase of PEO to lower frequency and becomes broad in shape for PEO-LiClO₄ systems. The peak intensity of the absorption bands of CH₂ stretching and CH₂ wagging of the crystalline phase of PEO reduces as the amount of the addition of LiClO₄ increases which indicates that the addition of LiClO₄ disrupted the ordering of the polymer chains of PEO and increases the amorphous of PEO. However, the

wavenumbers of PEO-LiClO₄ systems at all salt compositions are insignificantly shifting but the absorbances of these bands reduce as the content of LiClO₄ in the PEO matrix increases, which indicates qualitatively proportionate to the lower content of the crystalline phase in the PEO.

Nevertheless, the addition of nanofiller into PEO and PEO-salt systems only has substantial effects on the intermolecular interactions. The absorbance band of asymmetric and symmetric C-O-C stretching, CH₂ stretching and CH₂ wagging modes in terms of the peak intensity and their wavenumbers at all nanofiller compositions of PEO-TiO₂ and PEO-LiClO₄-TiO₂ systems remain unchanged as the amount of TiO₂ increases indicates that the crystalline phase of PEO is unaffected with the addition of nanofiller. Hence, it is confirmed that the addition of TiO₂ without any surface treatment into the PEO matrix did not have substantial effects on the molecular interaction between PEO and nanofiller in PEO-TiO₂ and PEO-LiClO₄-TiO₂ systems. It serves as a classical model of polymer-nanofiller systems with weak polymer-nanofiller molecular interaction. For future prospects, more studies on the surface modifications of TiO₂ are needed to improve the dispersion and interaction with the PEO matrix. Good dispersion and interaction between the TiO₂ filler and PEO

matrix will determine the performance of this composite and their practical applicability.

ACKNOWLEDGEMENTS

The authors sincerely acknowledge the late Prof. Dr. Melissa Chan Chin Han for her endless support and knowledge in this work.

REFERENCES

- [1] M.L. Verma, H.D. Sahu, *Ionics*. **23** (2017) 2339–2350.
- [2] A.R. Polu, H.-W.W. Rhee, *J. Ind. Eng. Chem.* **37** (2016) 347–353.
- [3] B.K. Bahuleyan, C. Induja, M.T. Ramesan, *Polym. Compos.* **40** (2019) 4416–4426.
- [4] Z. Zhao, W. Liang, S. Su, X. Jiang, Y. Bando, B. Zhang, Z. Ma, X. Wang, *Next Mater.* **7** (2025) 100364.
- [5] J. Li, X. Chen, S. Muhammad, S. Roy, H. Huang, C. Yu, Z. Ullah, Z. Wang, Y. Zhang, K. Wang, B. Guo, *Mater. Today Energy* **43** (2024) 101574.
- [6] A.R. Polu, S. Song, A.A. Kareem, S. V. Savilov, P.K. Singh, M. Venkanna, C.S. Kumar, *J. Phys. Chem. Solids* **196** (2025) 112319.
- [7] Y. He, Y. Dong, L. Qiao, C.M. Costa, S. Lanceros-Méndez, J. Han, W. He, *Energy Storage Mater.* **67** (2024).
- [8] D. Liu, X. Liu, L. Zheng, F. Chen, C. Guo, *Polymer*. **313** (2024) 127674.
- [9] S. Kozdra, M. Atsumi, *Mater. Today Commun.* **39** (2024) 109019.
- [10] Z. Li, P. Liu, K. Zhu, Z. Zhang, Y. Si, Y. Wang, L. Jiao, *Energy and Fuels* **35** (2021) 9063–9079.
- [11] J. Gurusiddappa, W.M.R.P. Suvama, K.P. Dasan, *Int. J. Innov. Res. Sci. Eng. Technol.* **4** (2015) 11447–11454.
- [12] R.C. Agrawal, G.P. Pandey, *J. Phys. D. Appl. Phys.* **41** (2008).
- [13] D.K. Pradhan, R.N.P. Choudhary, B.K. Samantaray, *Int. J. Electrochem. Sci.* **3** (2008) 597–608.
- [14] C.H. Chan, L.H. Sim, H.W. Kammer, W. Tan, N.H. Abdul Nasir, *Mater. Res. Innov.* **15** (2011) 2–5.
- [15] H. Ramli, C.H. Chan, A.M.M. Ali, *Macromol. Symp.* **382** (2018) 1–11.
- [16] J. Hu, W. Wang, B. Zhou, Y. Feng, X. Xie, Z. Xue, *J. Memb. Sci.* **575** (2019) 200–208.
- [17] S. Das, A. Ghosh, *AIP Adv.* **5** (2015).
- [18] D.K. Pradhan, R.N.P. Choudhary, B.K. Samantaray, *Mater. Chem. Phys.* **115** (2009) 557–561.
- [19] S.N.H.M. Yusoff, S.I.A. Halim, A.A.A. Tarmizi, N.F.A. Zainal, C.C. Han, *Macromol. Symp.* **408** (2023) 2200065.
- [20] S.N.H.M. Yusoff, S.I.A. Halim, A.A.A. Tarmizi, C.H. Chan, *Polym. Int.* **72** (2023) 935–948.
- [21] D. Zhou, D. Shanmukaraj, A. Tkacheva, M. Armand, G. Wang, *Chem* **5** (2019) 2326–2352.
- [22] S. Choudhary, R.J. Sengwa, *Electrochim. Acta* **247** (2017) 924–941.
- [23] M. Zhu, J. Wu, Y. Wang, M. Song, L. Long, S.H. Siyal, X. Yang, G. Sui, *J. Energy Chem.* **37** (2019) 126–142.
- [24] J.P. Sharma, N. Guleria, *J. Thermoplast. Compos. Mater.* **35** (2022) 1154–1168.
- [25] C.H. Chan, H.W. Kammer, *Ionics*. **22** (2016) 1659–1667.
- [26] A. Arya, A.L. Sharma, *J. Mater. Sci. Mater. Electron.* **29** (2018) 1–29.
- [27] S.I.A. Halim, C.H. Chan, T. Winie, *Macromol. Symp.* **371** (2017) 114–124.
- [28] K. Miguel I. Delgado Rosero; Nori M. Jurado Meneses; Ramiro Uribe, *Materials*. **12** (2019) 1464.
- [29] X. Yu, A. Manthiram, *Energy Storage Mater.* **34** (2021) 282–300.
- [30] H.P.S. Missan, B.S. Lalia, K. Karan, A. Maxwell, *Mater. Sci. Eng. B Solid-State Mater. Adv. Technol.* **175** (2010) 143–149.
- [31] A. Sil, R. Sharma, S. Ray, *Surf. Coatings Technol.* **271** (2015) 201–206.
- [32] S. Choudhary, R.J. Sengwa, *J. Appl. Polym. Sci.* **132** (2015) 1–12.
- [33] D.K. Pradhan, R.N.P. Choudhary, B.K. Samantaray, *Express Polym. Lett.* **2** (2008) 630–638.
- [34] M. Menisha, S.L.N. Senavirathna, K. Vignarooban, N. Iqbal, H.M.J.C. Pitawala, A.M. Kannan, *Solid State Ionics* **371** (2021) 115755.
- [35] L.H. Sim, S.N. Gan, C.H. Chan, R. Yahya, *Spectrochim. Acta - Part A Mol. Biomol. Spectrosc.* **76** (2010) 287–292.
- [36] M. Almakry, *Pure Appl. Sci.* **15** (2016) 24–35.
- [37] C.W. Lin, C.L. Hung, M. Venkateswarlu, B.J. Hwang, *J. Power Sources* **146** (2005) 397–401.
- [38] L. Kratofil Krehula, J. Stjepanović, M. Perlog, S. Krehula, V. Gilja, J. Travas-Sejdic, Z. Hrnjak-Murgić, *Polym. Bull.* **76** (2019) 1697–1715.
- [39] V.T. Nguyen, M. Tabish, G. Yasin, M. Bilal, T.H. Nguyen, C.P. Van, P. Nguyen-Tri, R.K. Gupta, T.A. Nguyen, *Nano-Structures and Nano-Objects* **25** (2021) 100671.
- [40] R.J. Sengwa, S. Choudhary, P. Dhatarwal, *J. Mater. Sci. Mater. Electron.* **30** (2019) 12275–12294.
- [41] M.J. O’Neil, *The Merck Index - An Encyclopedia of Chemicals, Drugs, and Biologicals*, 2013.
- [42] R.J. Seyler, *Assignment of the Glass Transition Temperature*, ASTM International, 1994.
- [43] C.T. Moynihan, M.A. Easteal, Bolt, J. Tucker, *J. Am. Ceram. Soc.* **59** (1976) 12–16.
- [44] S.I. Abdul Halim, C.H. Chan, H.-W. Kammer, *Polym. Test.* **79** (2019) 105994.
- [45] C.B. Roth, J.R. Dutcher, *Eur. Phys. J. E* **12** (2003) 103–107.
- [46] N.S. Hussin, F. Harun, C.H. Chan, *Macromol. Symp.* **376** (2017) 1–7.

- [47] S.I. Abdul Halim, C.H. Chan, J. Apotheker, *Chem. Teach. Int.* **3** (2021) 117–129.
- [48] K.H. Liao, S. Aoyama, A.A. Abdala, C. Macosko, *Macromolecules* **47** (2014) 8311–8319.
- [49] N.F.A. Zainal, H. Ramli, M. Fritz, V. Abetz, C.H. Chan, *Pure Appl. Chem.* **93** (2021) 1119–1139.
- [50] G. Foran, D. Mankovsky, N. Verdier, D. Lepage, A. Prébé, D. Aymé-Perrot, M. Dollé, *IScience* **23** (2020) 1–16.
- [51] S.K. Fullerton-Shirey, J.K. Maranas, *J. Phys. Chem. C* **114** (2010) 9196–9206.
- [52] S.K. Fullerton-Shirey, J.K. Maranas, *Macromolecules* **42** (2009) 2142–2156.
- [53] I.A. Tsekmes, R. Kochetov, P.H.F. Morshuis, J.J. Smit, in: 2013 IEEE Int. Conf. Solid Dielectr., IEEE, 2013, pp. 678–681.
- [54] D.M. Panaitescu, C. Radovici, M. Ghiurea, H. Paven, M.D. Iorga, *Polym. Plast. Technol. Eng.* **50** (2011) 196–202.
- [55] S. Choudhary, R.J. Sengwa, *Polym. Bull.* **72** (2015) 2591–2604.
- [56] S.N.H.M. Yusoff, S.I.A. Halim, N.F.A. Zainal, C.C. Tay, V. Abetz, C.H. Chan, (2024).
- [57] M. Perrier, S. Besner, C. Paquette, A. Vallée, S. Lascaud, J. Prud'homme, *Electrochim. Acta* **40** (1995) 2123–2129.
- [58] S. Besner, J. Prud'homme, *Macromolecules* **22** (1989) 3029–3037.
- [59] A. Ito, P. Phulkerd, V. Ayerdurai, M. Soga, A. Courtoux, A. Miyagawa, M. Yamaguchi, *Polym. J.* **50** (2018) 857–863.
- [60] S.I.A. Halim, C.H. Chan, L.H. Sim, *Macromol. Symp.* **365** (2016) 95–103.
- [61] P. Utpalla, S.K. Sharma, K. Sudarshan, V. Kumar, P.K. Pujari, *Eur. Polym. J.* **117** (2019) 10–18.
- [62] N.H. Gondaliya, D.K. Kanchan, P. Sharma, P. Joge, *Mater. Sci. Appl.* **02** (2011) 1639–1643.
- [63] T. Yoshihara, H. Tadokoro, S. Murahashi, *J. Chem. Phys.* **41** (1964) 2902–2911.
- [64] Y.L. Ni'Mah, M.Y. Cheng, J.H. Cheng, J. Rick, B.J. Hwang, *J. Power Sources* **278** (2015) 375–381.
- [65] S. Jayanthi, K. Kulasekarapandian, A. Arulsankar, K. Sankaranarayanan, B. Sundaresan, *J. Compos. Mater.* **49** (2015) 1035–1045.
- [66] C. Manoratne, R.M.G. Rajapakse, M.A.K.L. Dissanayake, *Int. J. Electrochem. Sci.* (2006).
- [67] H. Matsuura, T. Miyazawa, *J. Polym. Sci. Part A-2 Polym. Phys.* **7** (1969) 1735–1744.
- [68] B. Jinisha, A.F. Femy, M.S. Ashima, S. Jayalekshmi, *Mater. Today Proc.* **5** (2018) 21189–21194.
- [69] J. Ji, B. Li, W.H. Zhong, *Electrochim. Acta* **55** (2010) 9075–9082.
- [70] A. Dey, S. Karan, S.K. De, *J. Phys. Chem. Solids* **71** (2010) 329–335.
- [71] P. Dhatarwal, S. Choudhary, R.J. Sengwa, *Polym. Bull.* **78** (2021) 2357–2373.
- [72] G. Toskas, C. Cherif, R.D. Hund, E. Laourine, A. Fahmi, B. Mahltig, *ACS Appl. Mater. Interfaces* **3** (2011) 3673–3681.
- [73] S. Ketabi, K. Lian, *Electrochim. Acta* **154** (2015) 404–412.
- [74] F. Harun, C.H. Chan, T. Winie, *Polym. Int.* **66** (2017) 830–838.
- [75] R.J. Sengwa, P. Dhatarwal, *Electrochim. Acta* **338** (2020) 135890.
- [76] S.I.A. Halim, N.F.A. Zainal, C.H. Chan, J. Kressler, *Pure Appl. Chem.* **95** (2023) 755–777.

Direct Alcoholysis of Glucose into Alkyl Levulinates Catalysed by Metal-Doped Sulfonated Activated Carbon

Kirrthana Krishnasamy¹, Chee Shu Yi¹, Mohd Asmadi^{1*}, Zaki Yamani Zakaria¹, Muzakkir Mohammad Zainol², Sureena Abdullah³

¹ Faculty of Chemical and Energy Engineering, Universiti Teknologi Malaysia, 81310 Johor Bahru, Johor, Malaysia

² School of Chemical Engineering, College of Engineering, Universiti Teknologi Mara, 40450, Shah Alam, Selangor, Malaysia

³ Faculty of Chemical and Natural Resources Engineering, Universiti Malaysia Pahang, 26300, Gambang, Pahang, Malaysia

*Corresponding Author: mohdasmadi@utm.my

Article history:

Received 01 September 2024

Accepted 30 October 2024

ABSTRACT

Lignocellulosic biomass is widely studied to produce alkyl levulinate through acid catalyst catalysed alcoholysis, which potentially used as a biofuel additive. However, the poor properties of homogeneous catalyst have prompted this study to focus on enhancing the yield of alkyl levulinate by using sulfonated activated carbon (AC-S) doped with different metals as a heterogeneous catalyst with co-existence of Brønsted and Lewis acidic sites. The activated carbon (AC) precursor was modified via sulfonation and impregnated with iron (Fe), copper (Cu) and cobalt (Co) metals, which were further characterised to evaluate their physicochemical properties as a catalyst. Their catalytic activity was then evaluated for glucose alcoholysis in a stainless-steel batch reactor at 180 °C for 4 h, by charging 0.6 g of glucose, 40 mL of alcohol (methanol and ethanol) and 0.3 g of catalyst. According to the results, the catalysts' catalytic activity was improved after sulfonation and metal doping. Among the employed heterogeneous catalysts, AC-S-Cu exhibited the highest catalytic activity, which was contributed mainly by its co-existence of Brønsted and Lewis acidic sites with significant Brønsted acidity, higher thermal stability with minimum weight loss up to 200 °C (<2 wt%), better morphology, and larger surface area (928 m²/g) compared to other metal-doped AC-S. The maximum alkyl levulinate yield (15.04 wt%) was obtained for ethyl levulinate production under conditions of 180 °C, 4 hr, 0.6 g of glucose, 0.3 g of AC-S-Cu and 40mL of ethanol. The outcome of this study provides an insight on the potential of AC-S-Cu in facilitating the direct alcoholysis of glucose to alkyl levulinate.

Keywords: alkyl levulinate; Brønsted-lewis; alcoholysis; sulfonated activated carbon; metal doping

© 2024 Faculty of Chemical and Engineering, UTM. All rights reserved
| eISSN 0128-2581 |

1. INTRODUCTION

Climate change, energy security, and heavy dependence on fossil fuels are among global issues that require immediate attention. Biofuels have emerged as a sustainable alternative energy source via the use of biomass as a promising feedstock. Biomass mainly consists of cellulose, hemicellulose and lignin, often being utilized in the conversion of high value products such as levulinic acid (LA) and alkyl levulinate (AL) [1]. AL is a promising renewable fuel additive used to improve engine performance and produce greener emissions.

Due to the high chemical cost and complex synthesis route involving multiple steps from the easily accessible levulinic acid (LA) and furfuryl alcohol (FA) through esterification, the single-step approach of direct conversion of lignocellulose-derived sugars into AL has attracted interest [2]. As a result, monosaccharides like glucose is commonly used as a representative material for biomass

conversion studies as it is easier to be converted compared to polysaccharides and biomass which have stronger and more complex hydrogen bonds and Van Der Waals forces [3].

The direct AL production involves the esterification of monosaccharides with alcohol by employing acidic catalysts to promote the AL yields. Despite the cost-effectiveness and efficiency of the commonly used homogeneous catalyst such as sulfuric acid and hydrochloric acid, these acids present significant drawbacks related to environmental concerns such as lower recyclability and corrosion issues [4]. As an alternative, heterogeneous catalyst was introduced to tackle these issues. Various heterogeneous catalysts such as metal sulphates, sulphated metal chlorides, heteropolyacids, zeolites and resins have been previously employed in monosaccharides conversion to AL. However, those heterogeneous catalysts have drawbacks such as poor surface properties and fast catalyst deactivation [4]. As researches lately work towards

establishing green conversions, activated carbon (AC) is an emerging carbon-based heterogeneous catalyst. Activated carbons are well-known for their large surface area and adjustable surface functional groups providing specific properties, encouraged many researchers to employ it in the conversions of biomass to AL [5,6].

Many research projects have aimed to produce AL via heterogeneous acid catalyst with the combination approach of Brønsted-Lewis acids as they found that the combined effect of both acids have enhanced the reaction process by the following the pathway shown in Figure 1 [7]. The Brønsted-Lewis dual-acidity facilitates the glucose conversion to AL in such a pathway that requires lesser energy and hence enhances the AL yields [8]. This is in agreement with Tempelman et al. 2023 [5] which proved that the dual acidic tin-doped sulfonated activated carbon (Sn-Fn-AC) showed high activity towards the production of 5-HMF from glucose-fructose-sucrose aqueous solution as compared to the mono-acidic catalyst, where 30 mol% 5-HMF yield was obtained using Sn-Fn-Ac, while less than 5 mol% 5-HMF yield was reported using mono-acidic Fn-AC..

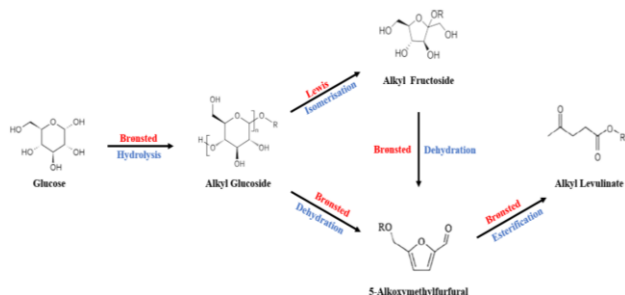


Figure 1. Roles of Brønsted and Lewis acid in facilitating AL conversions

Although several studies have employed AC-S in the biomass conversion to AL, research works on the employment of dual-acidity AC-S as a catalyst in direct glucose conversion to AL is scarcely reported. To the best of our knowledge, the synthesis of dual-acidity AC-S catalyst by metal doping with copper, cobalt and iron sulfates; and employing them in the direct glucose conversion AL have not been reported in literatures. Accordingly, this study aims to evaluate AL yield from direct glucose conversion through alcoholysis reaction catalyzed by newly developed catalysts. Sulfonation and metal doping were performed on the AC precursor to provide the joined acidities of Brønsted-Lewis. The catalysts were then characterized and employed in the conversion of glucose to two different ALs, namely methyl levulinate (ML) and ethyl levulinate (EL).

2. METHODOLOGY

All materials were purchased from Sigma Aldrich, VChem and Merck, ensured are analytical grade and were used as received. Commercialized activated carbon, concentrated sulfuric acid (H_2SO_4 , 95-97 %), iron (II) sulfate

heptahydrate ($\text{FeSO}_4 \cdot 7\text{H}_2\text{O}$), copper sulfate pentahydrate ($\text{CuSO}_4 \cdot 5\text{H}_2\text{O}$), cobalt sulfate heptahydrate ($\text{CoSO}_4 \cdot 7\text{H}_2\text{O}$) were used for the synthesization of heterogeneous catalyst. Meanwhile, pyridine was used for the catalyst characterization. The conversion of glucose to AL was conducted using methanol (CH_3OH), ethanol ($\text{C}_2\text{H}_5\text{OH}$, 95%), and glucose ($\text{C}_6\text{H}_{12}\text{O}_6$).

2.1 Catalyst Preparation

In this study, five different AC catalysts were prepared. In order to prepare AC-S, 10.0 g of AC was mixed with 100 mL of H_2SO_4 in 150 mL round bottom flask equipped with a magnetic stir bar and condenser. The mixture was then stirred at 300 rpm with heating at 373 K for 5 h. After the treatment, the mixture was diluted by adding 2 L of distilled water prior to vacuum filtration in a Büchner flask until the cleaning water pH was approximately 7. The sample was placed in a crucible and oven dried at 110 °C for 24 h. The dried sample was labelled as AC-S.

Next, the AC-S was further mixed with 10 g of $\text{FeSO}_4 \cdot 7\text{H}_2\text{O}$ which was pre-dissolved in 100ml distilled water in a 1 L beaker under 500 rpm stirring at room temperature for 2 h. The mixture was then filtered under suction and dried in the oven for 110 °C overnight before further calcined for 5 h at 300 °C. The dried sample was designated as AC-S-Fe. The same procedure was used to prepare AC-S-Cu and AC-S-Co using $\text{CuSO}_4 \cdot 5\text{H}_2\text{O}$ and $\text{CoSO}_4 \cdot 7\text{H}_2\text{O}$ respectively.

2.2 Catalyst Characterization

The thermal stability and degradation of the prepared catalysts were determined by Thermogravimetric Analysis (TGA) using TGA Q500 V20.13 Build 39 through inert heating from 30 to 950 °C with a heating rate of 10 °C/min. The presence of functional groups of catalyst was confirmed by Fourier transform infrared (FTIR) spectroscopy from Perkin Elmer Spectrum using KBr pellets in the IR range of 370 - 4000 cm^{-1} . Next, the catalyst's phase structure and crystallinity were studied via X-ray diffraction (XRD) analysis, which ranges from 3 ° to 100 ° 2θ with a step size of 0.02 ° and step time of 60 s, operated at 40 kV and 30 mA with a fixed 2/3° incident slit on the X-ray diffractometer (D/teX Ultra 250 Rigaku SmartLab with an attachment of ASC robot- reflection) via $\text{Cu K}\alpha$ radiation.

The elemental analysis and morphology of the samples were carried out using energy-dispersive X-ray (EDX) spectrometry coupled with Scanning Electron Microscopy (SEM) (Hitachi SU3500). The surface area and pore distribution were measured using Micromeritics 3-Flex instrument. The samples were degassed under vacuum at 200 °C for 6 h before conducting standard nitrogen (N_2) adsorption and desorption at -196 °C. The Brunauer-Emmett Teller (BET) method was used to calculate the total surface area, whereas Barrett-Joyner-Halenda (BJH) and t-plot methods were utilized to differentiate between the

micropores and mesopores volume associated with the surface area.

The acidity of the catalysts were determined by Ammonia-Temperature Program Desorption (NH₃-TPD) analysis. The analysis was conducted using Chemisorption Analyzer Micromeritics Autochem II, and degassing temperature was set at 150 °C. For the determination of acidity type for Brønsted-Lewis acid, the characterization was carried out using FTIR with pyridine as a probe. 50 mg of sample was dried at 115 °C for 1 h and cooled to room temperature, then 0.5 mL of pyridine was directly added into the sample in a glass vial and left for 1 h for a complete adsorption. The pyridine added sample was dried at 120 °C for 1 h then the sample was allowed to cool until room temperature. The dried sample was analyzed in the spectral region between 1400 and 1700 cm⁻¹ using alkali halide (KBr) pellets. The ratio of Brønsted to Lewis acid sites can be computed using Equation (1).

$$\text{Ratio of Brønsted to Lewis Acidity} = \frac{A_B \times C_L}{A_L \times C_B} \quad (1)$$

Where, A_B and A_L are the areas of Brønsted and Lewis acidity from FTIR (cm⁻¹), respectively, C_B and C_L is the coefficient of Brønsted and Lewis acidity (188 cm²/mmol) and (142 cm²/mmol).

2.3 Direct Alcoholysis of Glucose to AL

The alcoholysis of glucose was carried out in a 150 mL stainless steel batch reactor. The reactor was charged with 0.6 g of glucose, 0.3 g of AC and 40 mL of ethanol. The solution was then heated to 180 °C and stirred at 200 rpm for 4 h. Once the reaction was completed, the reactor was cooled to room temperature. The resulting reaction mixture was then filtered through a syringe filter (PTFE, 0.45 μm, VWR) prior to Gas Chromatograph-Flame Ionization Detector (GC-FID) analysis. Similar steps were taken for all AC-S, AC-S-Fe, AC-S-Cu and AC-S-Co to determine its catalytic activity. The experiment was repeated using methanol as solvent.

2.4 Product Analysis

To calculate the AL yields in the sample product, the resulting liquid undergoes analysis using GC-FID. The AL peak areas were identified using an Agilent Technology 7820A GC-FID system equipped with a DB-Wax column (30 m × 0.25 mm × 0.25 μm). The analysis conditions used were as follows: N₂ as the carrier gas with 1.0 mL/min of flow rate, the injection port temperature of 250 °C, the detector temperature of 270 °C, and the oven temperature programmed from 50 to 170 °C (5 °C/min), followed by 170-240 °C (15 °C/min). Standard calibration curve of AL standard solution was constructed to derive the equation for ALs concentration calculation in the product sample. The ALs yields were calculated using Equation (2).

ALs Yield (wt %) =

$$\frac{\text{Concentration of ALs} \left(\frac{g}{mL}\right) \times \text{Volume of product (mL)}}{\text{Amount of Initial Glucose (g)}} \times 100\% \quad (2)$$

3. RESULTS AND DISCUSSION

3.1 Catalyst Characterization

The TGA/DTG curve is shown in Figure 2a. Activated carbon exhibits lowest thermal stability due to its lower activation energy for oxidation of amorphous structure [1], whereby its thermal stability increases after sulfonation as AC is affected by strong acid on the carbon structure. Further modification of AC-S with metal doping increases the thermal stability of the sample, which was contributed by the high thermal stability of metals itself [7]. It is observed that 2.5 wt% weight loss in the 270–330 °C temperature region, which could be attributed to decomposition of the –SO₃H groups [5]. Since the alcoholysis reaction was carried out at 180 °C, all the metal doped sulfonated activated carbon showed good thermal stability up to 400 °C and are suitable to be employed in the conversion process as there is no drastic weight loss indicated in TGA curves below 180 °C.

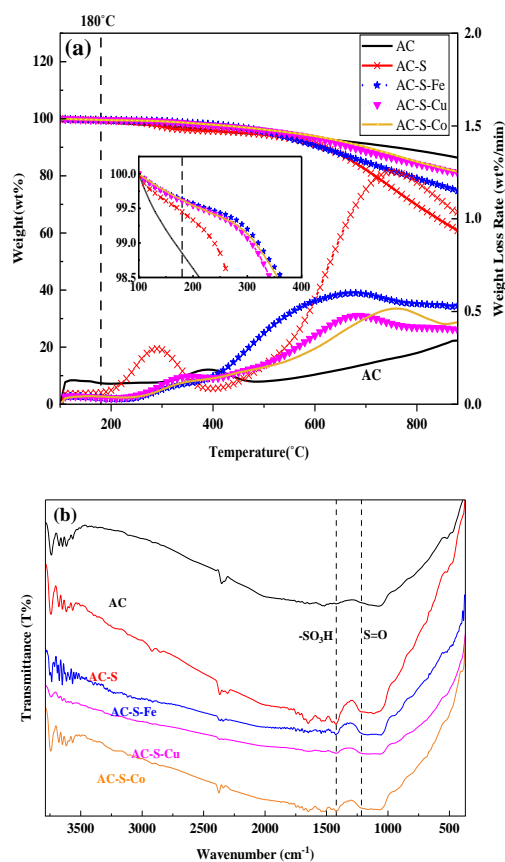


Figure 2. (a) TGA-DTG thermographs and (b) FTIR spectra of AC, AC-S, AC-S-Fe, AC-S-Cu and AC-S-Co

Figure 2b represents the FTIR spectra of the catalysts. A distinct vibration is evident between 3800 cm^{-1} and 3500 cm^{-1} , indicating O-H stretching and the generation of hydroxyl groups, along with adsorbed water on the surface of the carbon [9]. The existence of S=O stretching and $-\text{SO}_3\text{H}$ bonding in the range of 1350 cm^{-1} and 1020 cm^{-1} corresponds to the introduction of SO_3H groups, which signifies the effective attachment of $-\text{SO}_3\text{H}$ groups onto the activated carbon surface in all the catalysts except AC. For samples doped with metal, a noticeable peak appears within the range of 570 cm^{-1} to 400 cm^{-1} . Two additional small peaks at 384 cm^{-1} and 400 cm^{-1} were identified indicating the presence of Fe-O and Co-O bonds respectively following the impregnation process [2,10].

The crystallinity of prepared catalysts was observed using XRD analysis and the spectrum derived is depicted in Figure 3a. All the synthesized carbon materials display two well-defined diffraction peaks at 2θ angles around 23° and 42° , with varying intensities, which indicated a disordered activated carbon sheet structure. There are minor crystal peaks in the range of 30° to 40° associated with iron oxide (FeO). This is attributed to the interaction between the Fe species and the AC-S structure, resulting in reduced crystallinity of the amorphous peak which agrees with the literature data [7].

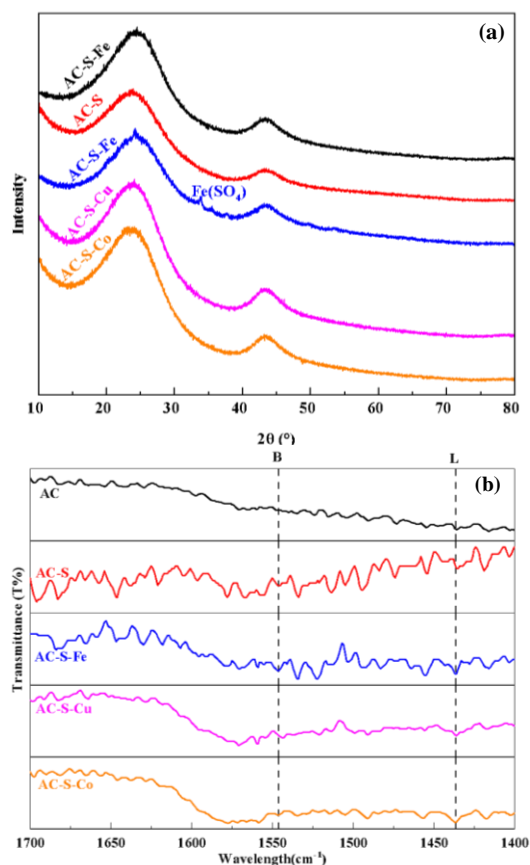


Figure 3. (a) XRD and (b) Pyridine-FTIR spectra of AC, AC-S, AC-S-Fe, AC-S-Cu and AC-S-Co (B: Brønsted, L: Lewis)

However, the small peak of metal elements was not clearly observed by both FTIR and XRD spectrums, which could be due to the presence of low Fe, Cu and Co species on the AC-S structure. The existence of $-\text{SO}_3\text{H}$ and metal elements on the surface of the activated carbon was confirmed through EDX analysis, as tabulated in Table 1. The presence of sulfur (S) in the AC-S sample confirmed the successful sulfonation of the activated carbon. The trace amount of sulfur in the AC sample may be attributed to contamination during sample preparation. Additionally, the detection of Fe, Cu, and Co elements in the AC-S-Fe, AC-S-Cu, and AC-S-Co samples respectively indicates the effective and uniform doping of each metal onto the activated carbon surface.

Table 1: Composition of element contained in AC, AC-S, AC-S-Fe, AC-S-Cu and AC-S-Co

Catalyst	Element Weight (%)						
	C	O	S	Fe	Cu	Co	N
AC	87.0	12.1	0.8	-	-	-	0.1
AC-S	87.7	10.1	2.2	-	-	-	
AC-S-Fe	68.6	11.7	2.0	17.7	-	-	0.1
AC-S-Cu	83.9	6.2	1.4	-	8.2	-	0.3
AC-S-Co	86.4	8.1	1.3	-	-	3.9	0.3

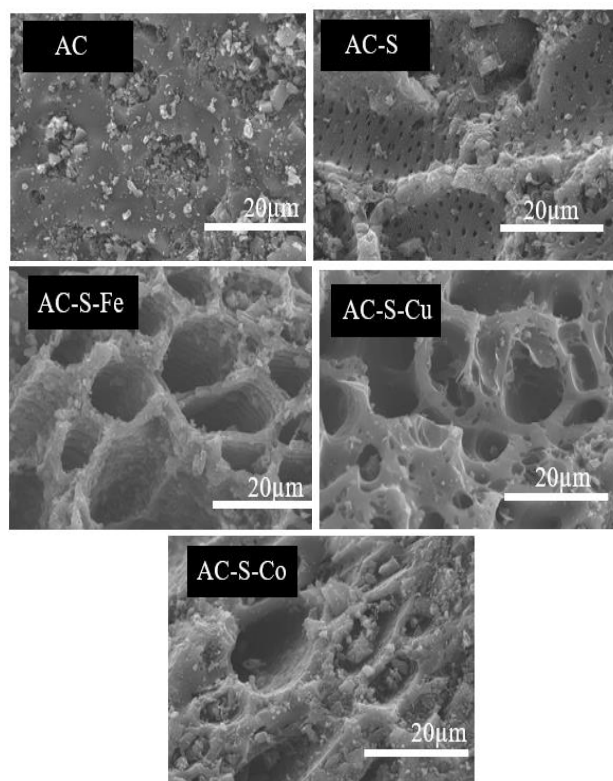


Figure 4. SEM images of AC, AC-S, AC-S-Fe, AC-S-Cu and AC-S-Co

Figure 3b shows the pyridine-FTIR spectra of the prepared catalysts. An absorption peak near 1450 cm^{-1} indicates the presence of Lewis acidic sites, whereas an absorption peak near 1540 cm^{-1} represents Brønsted acidic sites [14,15]. The Brønsted to Lewis ratios of AC, AC-S, AC-S-Fe, AC-S-Cu and AC-S-Co were calculated to be 0.48, 1.51, 0.73, 0.81 and 0.66. The introduction of sulfonic acid increases the B/L ratio due to the contribution of Brønsted acid sites increases. The B/L ratio decreases after metal doping attributed to the significant presence of strong Lewis acidic metals.

The surface morphology of prepared catalysts is presented by SEM images in Figure 4. The irregular particles with a rough surface are observed for all samples suggested that activated carbon exhibited numerous micropores on the surface, ultimately contributing to an increased material surface area. The high acid treatment during sulfonation process leads to some development of tiny pores, which exposes a larger surface area for reactions. In addition, the metal doped ACs showed better morphology than AC due to the more open structure for the reaction with the formation of acid sites.

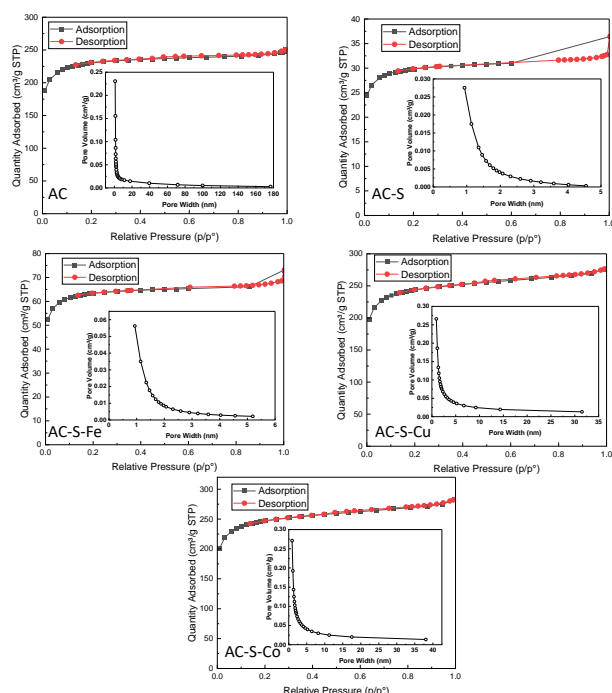


Figure 5. N_2 adsorption-desorption isotherms and BJH pore size distributions of AC, AC-S, AC-S-Fe, AC-S-Cu and AC-S-Co

Surface area and porosity of the catalyst are other major factors influencing catalytic activity in providing high EL yield. Figure 5 displays the N_2 adsorption-desorption isotherms and pore size distribution. The isotherms obtained for the synthesized catalysts fit the II-type adsorption and correspond to an H4-type hysteresis loop based on the IUPAC classification as expected from literature data [11]. This indicates the formation of microporous structures and

the existence of aggregates of plate-like particles, leading to the creation of slit-shaped pores with irregular sizes and shapes. Table 2 and 3 summarizes the surface area and porosity of the catalysts. The parent material (AC) contains a BET surface area of $881\text{ m}^2/\text{g}$, which decreases to $114\text{ m}^2/\text{g}$ after sulfonation and increases again after introduction of metals. This decrease indicates SO_3H groups were added not only to the surface of the AC material but also occupied some of the pore openings, as proved by the previous findings [4,12]. A subsequent increment in S_{BET} and V_{pore} was observed after metal doping. The addition of metals in the forms of nanoparticles after metal-doping prevents the agglomeration of carbon particles, resulting in a more dispersed structure by having increased volume of micropores, and thus the surface area increases [6,13]. Catalyst with higher surface area is always preferred for catalytic reactions as they have more available active sites for the reaction to take place, and thus more reaction can occur simultaneously leading to higher product yields. This trend was aligned with the SEM result, where the metal-doped AC-S was more porous, which exposed more active sites and favors the reaction.

Table 2: Surface area and porosity of AC, AC-S, AC-S-Fe, AC-S-Cu and AC-S-Co

Catalyst	Surface Area (m^2/g)		
	S_{BET}^a	S_{Meso}^b	S_{Micro}^c
AC	881	213	667
AC-S	114	27	87
AC-S-Fe	243	52	191
AC-S-Cu	929	237	691
AC-S-Co	939	248	692

^a BET surface area was obtained from the N_2 adsorption isotherm.

^b Surface areas of mesopore were obtained from the t-plot method.

^c Surface areas and pore volume of micropore were obtained from the t-plot method.

Table 3: Porosity of AC, AC-S, AC-S-Fe, AC-S-Cu and AC-S-Co

Catalyst	Pore volume (cm^3/g)			Pore diameter (nm)
	V_{Pores}^a	V_{Meso}^b	V_{Micro}^c	
AC	0.39	0.12	0.27	1.75
AC-S	0.05	0.02	0.03	1.78
AC-S-Fe	0.11	0.03	0.08	1.75
AC-S-Cu	0.43	0.15	0.28	1.84
AC-S-Co	0.44	0.16	0.28	1.86

^a Pore volume was obtained from the single-point desorption method.

^b Volume of mesopore = ($V_{\text{pores}} - V_{\text{micro}}$).

^c Estimated from the adsorption average pore diameter ($4 V/A$ by BET).

^d Estimated from the BJH desorption average pore diameter ($4 V/A$).

The NH_3 -TPD profiles of the five different catalysts is depicted in Figure 6 and their acidity values are shown in Table 4. The desorption temperature and the intensity of the peaks is associated with the catalysts' acidic number and strength. Desorption peak below $200\text{ }^\circ\text{C}$ indicates the presence of weak acidic sites, $200\text{-}600\text{ }^\circ\text{C}$ indicates the

presence of moderate acidic sites, while desorption peak above 600°C indicates presence of strong acidic sites. AC has the lowest acidity with low intensity peaks observed. AC-S has slightly higher acidity, with higher intensity peak at weak and moderate acidic sites regions. The sulfonation performed on AC had contributed to the increase in catalyst acidity but still weak. Interestingly, upon metal-doping the catalysts' acidities greatly enhanced with AC-S-Co and AC-S-Cu reported the highest acidity of 2.81 and 2.69 mmol/g, respectively. Highest intensity peaks under all regions were observed in the NH₃-TPD profiles of the metal-doped catalysts. The metal doping had successfully enhanced the catalyst acidity contributed by the joined Brønsted and Lewis acidity, as hypothesized. According to the acidity values reported in Table 4, the order of catalyst acidity can be arranged as AC-S-Co ≈ AC-S-Cu > AC-S-Fe > AC-S > AC.

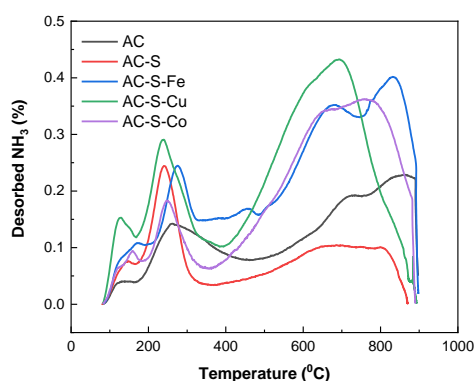


Figure 6. AC based catalysts' acidity based on NH₃-TPD profiles.

Table 4. Acidity values of AC based catalysts

Catalysts	Weak acidity (mmol/g)	Moderate acidity (mmol/g)	Strong acidity (mmol/g)	Total acidity (mmol/g)
AC	0.09	0.33	0.65	1.08
AC-S	0.42	0.58	0.62	1.62
AC-S-Fe	0.36	0.49	0.84	1.68
AC-S-Cu	0.29	1.93	0.48	2.69
AC-S-Co	0.06	0.19	2.56	2.81

3.2 Direct Alcoholysis of Glucose to AL

The AL yields obtained from glucose using these five catalysts are illustrated in Figure 7. Activated carbon acting alone as a catalyst, presented poor catalytic activity in the glucose conversion to ALs. The poor catalytic activity of AC is attributed to the absence of acidic sites in the catalyst, which is one of the main factors to facilitate ALs production from biomass carbohydrates. Fortunately, upon sulfonation the AC's catalytic activity has greatly enhanced with

reported ML and EL yields of 9.87 wt% and 4.21 wt%, respectively. Brønsted acidic sites was introduced in the AC upon sulfonation, which favors the dehydration and esterification reactions that will accelerate the yielding of targeted ALs.

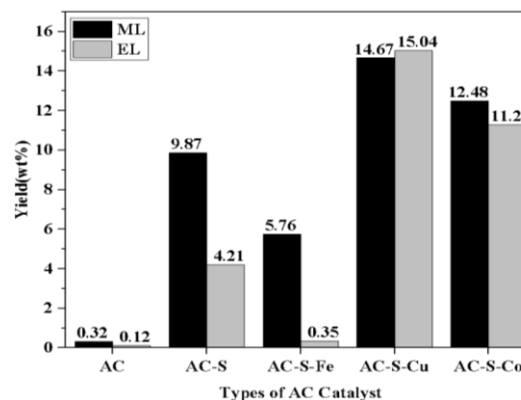


Figure 7. Alkyl levulinate yields obtained from different activated carbon catalysts (180 °C, 4 h, 0.6 g glucose, 0.3 g AC catalyst, 40 mL alcohol)

Interestingly, incorporation of metals in the AC-S had improved the AL yields for AC-S-Cu (ML: 14.67 wt%; EL: 15.04 wt%) and AC-S-Co (ML: 12.48 wt%; EL: 11.28 wt%), but reduced for AC-S-Fe (ML: 5.76 wt%; EL: 0.35 wt%). The addition of metals in the AC-S had formed catalysts with Brønsted-Lewis dual acidities, which further promoted the AL yields. AC-S-Cu exhibited the highest catalytic activity among all which was mainly due the combination of Brønsted-Lewis acidic sites with the significant Brønsted acidity, supported by the higher surface area and porosity, had increased the selectivity of AL production and further contributed to the higher AL yields [16,17]. In comparison between AL yields obtained from AC-S and AC-S-Fe, the AL yields reduced when AC-S-Fe was employed as catalyst, contradict to the hypothesis made where Brønsted-Lewis dual acidity could enhance the AL yields. As can be observed in Table 4, AC and AC-S-Fe have almost similar total acidities, however the weak and moderate acidic sites of AC are much higher compared to AC-S-Fe. Very strong acidity could shift the reaction pathway of glucose conversion to other by-products and cause high etherification of alcohol leading to solvent loss, and thus resulting in a lower yield [18]. Similar trend can be observed between AC-S-Cu and AC-S-Co, where although AC-S-Co has higher total acidity, AC-S-Cu's higher moderate acidic sites were more favourable for AL production. This elucidates that although acidic sites are required for AL production from biomass carbohydrates, it is important to properly tune the catalyst acidity as very high or very low acidity could lead to low AL yields. According to the observations made in this study, the glucose conversion to AL is preferable using catalyst with moderate acidity.

4. CONCLUSION

[18] G. Wang, Z. Zhang, L. Song, (2014) 1436.

The highest AL yields (ML: 14.67 wt%, EL: 15.04 wt%) obtained from glucose conversions were using Brønsted-Lewis AC-S-Cu under conditions of 180 °C, 4 h, 0.6 g of glucose loading, 40 mL of ethanol and 0.3 g of AC-S-Cu. The Brønsted-Lewis dual acidity with significant Brønsted acid value of AC-S-Cu as detected in pyridine FTIR analysis, had greatly contributed to its high catalytic activity. The larger surface area and porosity are also a major factor in providing high AL yield. Thus, it can be deduced that AC-S-Cu is a potential catalyst that had exhibited its prominence in the direct alcoholysis of glucose to AL.

ACKNOWLEDGEMENTS

This work was sponsored by Universiti Teknologi Malaysia Fundamental Research (UTM FR) grant [Q.J130000.3846.22H57] and partly supported by Ministry of Higher Education Malaysia (MOHE) under the Fundamental Research Grant Scheme [FRGS/1/2020/TK0/UTM/02/1].

REFERENCES

- [1] S. Wang, K. Komvopoulos, *Sci Rep* (2021) 3914.
- [2] S.G. Krishnan, F.L. Pua, K. Palanisamy, S.N.S. Jaafar, K. Subramaniam, (2018) 870.
- [3] Z Mohammadbagheri, A.N. Chermahini, (2020) 2229.
- [4] Q. Guan, T. Lei, Z. Wang, H. Xu, L. Lin, G. Chen, X. Li, Z. Li, (2018) 150.
- [5] C. Tempelman, U. Jacobs, J. Herselman, R.V. Driel, F. Schraa, J. Versijde, T.V. Waversveld, Y. Yagci, M. Barg, F. Smits, F. Kuijpers, K. Lamers, T. Remijn, V. Degirmenci, (2023) 106661.
- [6] S.A. Sadeek, E.A. Mohammed, M. Shaban, M.T.H.A. Kana, N.A. Negm, (2020) 112749.
- [7] M.M. Zainol, M. Asmadi, P. Iskandar, W.A.N.W. Ahmad, N.A.S. Amin, T.T. Hoe, (2021) 124686.
- [8] M. Wang, L. Peng, X. Gao, L. He, J. Zhang, (2020) 1383.
- [9] N. Ya'aini, G.K.A Pillay, A. Ripin, 7th CONCEPT, 27-28 November 2018, Johor, Malaysia, 2019, p. 90.
- [10] T.M. Masikhwa, J.K. Dangbegnon, A. Bello, M.J. Madito, D. Momodu, N. Manyala, (2016) 60.
- [11] C. Fan, V. Nguyen, Y. Zeng, P. Phadungbut, T. Horikawa, D. Do, D. Nicholson, (2015) 79.
- [12] W. Gong, C. Chen, Y. Zhang, H. Zhou, H. Wang, H. Zhang, Y. Zhang, G. Wang, H. Zhao, (2017) 2172.
- [13] S.Y. Lee, S.J. Park, (2012) 307.
- [14] J. Heda, P. Niphadkar, V. Bokade, (2019) 2319.
- [15] C. Chang, L. Deng, G. Xu, (2018) 197.
- [16] A.H. Hassan, M.M. Zainol, K.R. Zainuddin, H.A. Rosmadi, M. Asmadi, N.A. Rahman, N.A.S. Amin, (2022) 264.
- [17] F. Yang, J. Tang, (2019) 1403.